Full Band Schrodinger Poisson Solver for DG SOI MOSFET

by

Akash Laturia

A Thesis Presented in Partial Fulfillment
of the Requirements for the Degree
Master of Science

Approved November 2016 by the
Graduate Supervisory Committee:

Dragica Vasileska, Chair
David Ferry
Stephen Goodnick

ARIZONA STATE UNIVERSITY

December 2016

ABSTRACT

Moore's law has been the most important driving force for the tremendous progress of semiconductor industry. With time the transistors which form the fundamental building block of any integrated circuit have been shrinking in size leading to smaller and faster electronic devices.As the devices scale down thermal effects and the short channel effects become the important deciding factors in determining transistor architecture.SOI (Silicon on Insulator) devices have been excellent alternative to planar MOSFET for ultimate CMOS scaling since they mitigate short channel effects. Hence as a part of thesis we tried to study the benefits of the SOI technology especially for lower technology nodes when the channel thickness reduces down to sub 10nm regime. This work tries to explore the effects of structural confinement due to reduced channel thickness on the electrostatic behavior of DG SOI MOSFET. DG SOI MOSFET form the Qfinfet which is an alternative to existing Finfet structure. Qfinfet was proposed and patented by the Finscale Inc for sub 10nm technology nodes. As part of MS Thesis we developed electrostatic simulator for DG SOI devices by implementing the self consistent full band Schrodinger Poisson solver. We used the Empirical Pseudopotential method in conjunction with supercell approach to solve the Schrodinger Equation. EPM was chosen because it has few empirical parameters which give us good accuracy for experimental results. Also EPM is computationally less expensive as compared to the atomistic methods like DFT(Density functional theory) and NEGF (Non-equilibrium Green's function). In our workwe considered two crystallographic orientations of Si,namely [100] and [110].

Dedicated to my parents and teachers

ACKNOWLEDGMENTS

This project was ideated by startup company named Finscale and wholly motivated by my advisor Prof. Vasileska. Without her support it would have been impossible to complete this MS thesis. Her trust and confidence in me helped me successfully accomplish the project goals. The qualities learnt from her during the course of my thesis work has helped me shape my career and made me a better person. I would also like to immensely thank Prof. Massimo Fischetti, Material Science Department, University of Texas Dallas without whom this project would not have been successful. Discussions with him helped me understand the physics related to thin film devices better. I am very grateful that he was patient and generous with me through all my interactions with him.

I am grateful to Prof. Ferry and Prof. Goodnick for being a part of my Graduate Advisory Committee. I would like to thank School of Electrical and Computer Engineering at ASU for providing me the opportunity to pursue Master of Science degree. I would also like to thank all my research group members for being supportive and special thanks to Dr. Raghuraj Hathwar for some insightful discussions regarding thesis topic. I am grateful to my academic advisor Toni Mengret for helping me out with all the administrative formalities. I am totally indebted to my family for the love and support I received in my quest for higher education.

TABLE OF CONTENTS

CHAPTER

CHAPTER Page

APPENDIX

LIST OF TABLES

LIST OF FIGURES

Figure Page

Chapter 1

INTRODUCTION

Semiconductors have led to industrial revolution in todays's society. It has changed the way humans lead their lives. Semiconductors have empowered the computers and other computing platforms with immense capability that altered the course of human history. One of the things that has been constant with the semiconductor industry is the change. The constant pursuit of reduction in transistor sizes has been the driving factor for the semiconductor industry. Famously called as Moore's law [2] it states that "The number of transistors incorporated in a chip will approximately double every 24 months."This has led to constant reduction in size of transistors leading to increased density of transistors per unit die area.

As we go down the scaling path for the conventional bulk planar MOSFET short channel effects and channel to drain capacitance starts increasing. These factors limit the performance of the planar MOSFET in the deep nanoscale regime. To reduce the short channel effects and increased leakage due to tunneling between the gate(physically thick but electrically thin) and the semiconductor through the oxide we need to use channels with higher levels of doping and high dielectric materials for gate [4]. Alternate device architectures need to be considered for continuing the CMOS scaling. Fig.1.2 represents the different device architectures being considered to continue Moores' law.

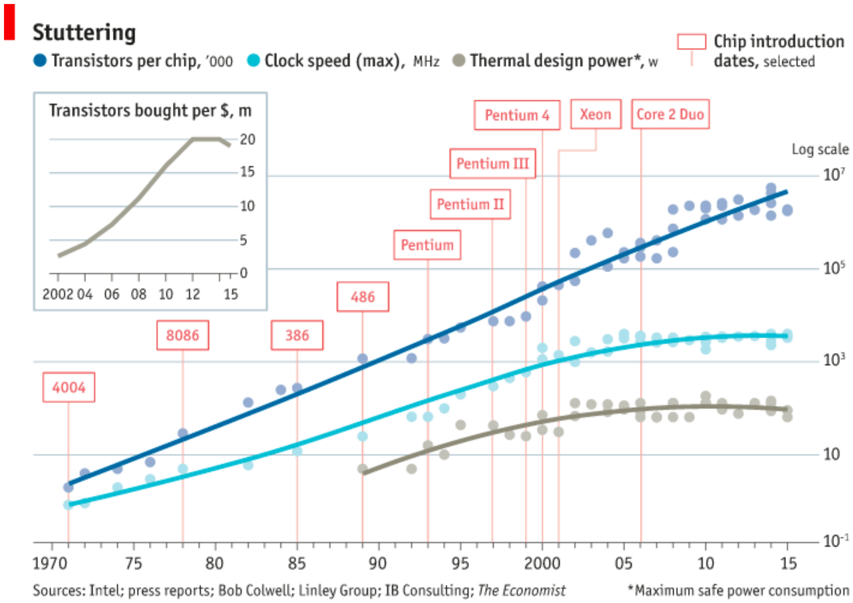

Figure 1.1: Moore's Law

Fig. Courtesy @ [3]

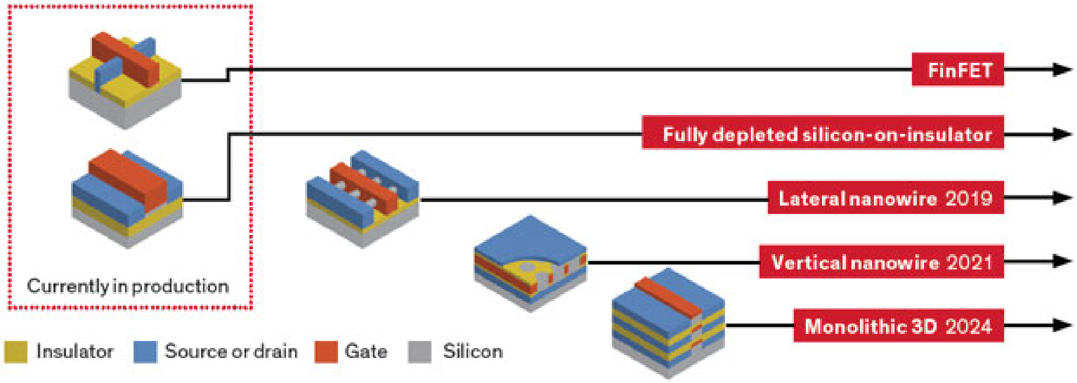

Figure 1.2: Transistor Architectures

Fig. Courtesy @ [5]

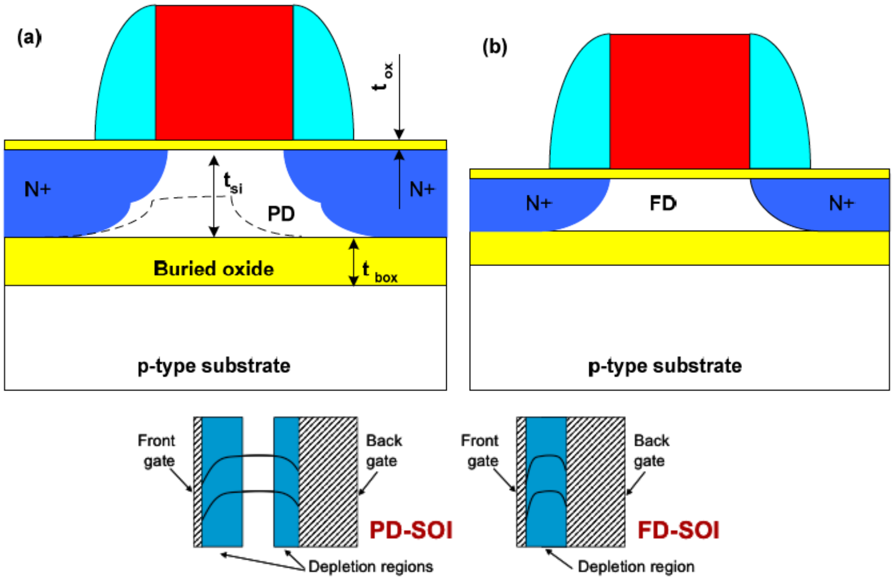

Figure 1.3: SOI MOSFET

Fig. Courtesy @ [9][10]

1.1 Device Architectures to Continue Moore's Law

As is depicted in Fig.(1.3) SOI MOSFET offer a better alternative to continue the Moore's law for lower technology nodes. Due to the buried oxide layer they have reduced parasitics and have better short channel behavior as compared to planar MOSFET [6]. One of the major benefits of SOI MOSFET is that they are easy to fabricate and no elaborate changes are required to the existing production capability [7]. Also SOI MOSFET provide advantages such as absence of latch up,reduced power consumption due to improved current carrying capability and better reliability than their bulk CMOS counterparts.The elimination of the reverse body effect in stacked digital circuit applications [8] is also another advantage of SOI over bulk transistors.

1.2 UTB SOI DEVICES

There are two types of SOI devices: a.)PDSOI(Partially Depleted Silicon on Insulator) b.)FDSOI(Fully Depleted Silicon on Insulator).In PD SOI the silicon body is thicker than the gate depletion width so that the depletion layer covers partially the space under the gate, while in FD SOI the silicon layer thickness is smaller or equivalent to the depletion width; hence the name fully depleted SOI [10]. PDSOI has its own advantages over conventional bulk MOSFET. It leads to 20% increase in performance,50% reduction in power consumption for same operating voltage,radiation hardness,etc.[11] One of the major structural disadvantage in PDSOI devices is floating body due to larger thickness of Si channel. Floating body leads to unstable threshold voltage due to variation of substrate to source voltage, increase in the drain current near saturation region also known as kink effect and switching memory effects causing delay variations in circuit. One of the ways to reduce the floating body effect is to use smaller thickness of Si channel region leading to class of devices known as FDSOI.The thickness of Si channel in FDSOI is less than the depletion width.

1.3 Exploration of UTB SOI: Experimentally and Theoretically

Ultra Thin Body SOI (UTB SOI)devices are future of CMOS scaling [12].They are extension of scaling FDSOI technology. These devices provide advantage in terms of area occupied on the die leading to increased density. Also these devices have added structural confinement due to the reduced thickness of Silicon layer which enhances the mobility. The carrier distribution is shifted more into the depth of the channel rather being close to the surface. This leads to improved current density in UTB SOI devices.UTB SOI Devices also have comparatively smaller junction area leading to smaller junction capacitance thereby increasing control of the gate over channel.

In the past there have been studies of UTB SOI devices to gauge the benefits of using thin layer of silicon channel. Experimental studies on UTB SOI pMOSFET have shown that the mobility increases with the reduction in the silicon film thickness [13]. Also it has been experimentally demonstrated that [110] oriented Si UTB SOI MOSFET has better performance over its [100] counterpart [13] for reduced channel thickness. Attempts have also been made at modeling the UTB SOI devices to understand the electron transport and predict with certain degree of accuracy about its performance for lower technology nodes [14]. Electrostatic modeling of these devices will help us optimize their design for lower technology nodes. Approaches to modeling UTB SOI used effective mass theory to estimate their performance or Monte Carlo study with quantum corrected potential [15]. Effective mass theory and Monte Carlo with quantum corrected potential do not accurately explain the quantum confinement effects on charge distribution and potential in channel region. These approaches also do not take into account the atomic potential fluctuations. Quantum confinement effects and the fluctuations in atomic potential start to manifest itself as the thickness of Si channel is reduced. Hence we adopted the full band approach to study the effect of structural confinement on band-structure of silicon slabs.

1.4 Organization of Thesis

As effective mass approach fails to describe the device behavior for reduced channel thickness and all crystallographic orientation we adopted atomistic approach to modeling. For modeling purposes we have selected UTB SOI n-MOSFETS. This model can be easily extended for UTB p-MOSFET as well. Device under study is the symmetric DG SOI architecture. The details of the model we developed are described in the following chapters:

- **Chapter 2**: This chapter discusses the supercell approach deployed along with

Empirical Pseudopotential method (EPM) to calculate the band-structure of UTB SOI devices. Band-structure is computed for two crystallographic orientation namely [100] and [110]

- **Chapter 3**: In this chapter we extract the wavefunction of electrons and holes from EPM . Since EPM is a k-space method hence it is necessary to transform the wave-function from k-space to real space to be useable to setup the Poisson equation in real space. We also compute the Density of States (DOS) from full band-structure for charge calculation purposes.

- **Chapter 4**: This chapter describes how the Poisson solver is setup to couple self- consistently with Schrodinger solver to get charge and potential through the device. Implementation details of self consistent full band Schrodinger Poisson solver are also explained.

- **Chapter 5**: The model developed in previous chapters enabled study of equilibrium properties of UTB SOI as function of parameters such as thickness of silicon channel, doping concentration, gate voltage and crystallographic orientation. Properties such as threshold voltage, charge distribution profile and capacitance have been analyzed for UTB SOI devices as function of afore mentioned parameters. This chapter describes the results obtained through simulation.

- **Chapter 6**: Scope for future work and conclusions are discussed.

Chapter 2

STRUCTURAL CONFINEMENT EFFECTS ON BAND-STRUCUCTRE

2.1 Motivation for Atomistic Approach

To model the equilibrium properties of UTB SOI against variables like silicon channel thickness, doping concentration and crystallographic orientation the widely adopted method is effective mass Schrodinger equation coupled with Poisson solver.

$$\frac{-\hbar^2}{2m_e^*}\nabla^2\boldsymbol{\psi(z)} + V(z)\boldsymbol{\psi(z)} = E\boldsymbol{\psi(z)} \tag{2.1}$$

$$\begin{aligned} \frac{d^2\boldsymbol{\phi}}{dz^2} &= \frac{e(n(z) - p(z) + Na - Nd)}{\boldsymbol{\epsilon}} \\ V(z) &= -e\boldsymbol{\phi}(z) \end{aligned} \tag{2.2}$$

In Eq.(2.1) m_e^* is the electron effective mass whereas $n(z)$ and $p(z)$ in Eq.(2.2) represent the electron and hole concentration respectively. Since $n(z)$ and $p(z)$ are dependent on the solution of Eq.(2.1) which in turn is dependent on potential that is calculated using Eq.(2.2). Thus Eq.(2.1) and Eq.(2.2) are solved self consistently to find the charge distribution in the device and the corresponding potential profile.

Effective mass equation (EME) assumes parabolic $E - k$ relationship. For [100] oriented Si n MOSFET EME has been successful in modeling the quantum transport in inversion layers with reasonable accuracy [16][17]. But there are certain limitations when the method is applied for holes. Firstly since holes have non- parabolic bandstructure due to warping of valence bands. In addition for [110] oriented Si there is added complexity in using EME since the principle axes of devices (confinement direction and the width) are not aligned with the principle axes of constant energy ellipsoids. Due to non alignment the effective mass equation become enormously complicated. EME does not take into account the added structural confinement in UTB SOI devices caused due to limited thickness of Silicon channel t_{si}[18].

As is known, effective-mass-approach is an approximation which disregards the atomic scale fluctuation of the electronic characteristics and describes the band edge electronic properties in an approximate manner[18]. However, as thickness of the silicon channel goes down, the behavior of the electronic states in nanoscale CMOS devices become more and more sensitive to all sorts of microscopic phenomena: atomic-scale fluctuations, local bond distortions, alloy effects, structure of the interfaces, quantum tunneling and energy quantization. Also the complete nature of the band edge electronic properties of the material cannot be described by just introducing a non-parabolicity factor. An improved modeling of such effects is not possible within effective mass approach and a full band atomistic treatment is necessary to address them.

Semi-empirical tight binding method and Empirical Pseudo-potential method (EPM) are two methods employed to do full band analysis. Tight binding method using s, p and d atomic orbitals basis has been already applied to 1D simulation of resonant tunneling diode (RTD) and zero dimensional quantum dot [19]. Since tight binding uses limited number of atomic basis function there is little variational flexibility for determining the conduction band energy and wavefunction [1]. Also the atomic basis function cannot correctly describe the electron wavefunction in between atoms; where it behaves more like free electron. Tight bindidng method does not explicitly use the atomic bsis functions but rather uses empirically adjusted parameters for elecrtonic structure calculation. This makes it difficult to model semiconductor surfaces [1]. All these limitations can be overcome by using the pseudopotentials. Tight binding is a real space approach as opposed to EPM which is reciprocal space approach to band-structure calculation. Thus EPM can be easily scalable to 2 or 3 dimensions.Both tight binding and EPM are empirical methods where the parameters can be empirically fitted to explain the experimental data. As opposed to empirical method there are ab initio methods like Density functional Theory and Hartree Fock method which do not require any empirically fitted parameters and treat electron electron interaction as well. But these methods are computationally expensive as opposed to empirical methods.

2.2 Empirical Pseudopotential Method

For general n electron system the Schrodinger equation is described as follows :

$$\begin{aligned}&\Big[\sum_{\boldsymbol{i}}\frac{p_i^2}{2m_o}+\sum_{\boldsymbol{i,j,l}}V_{\boldsymbol{\alpha}}(r_i-R_{l\boldsymbol{\alpha}})+\frac{1}{2}\sum\nolimits_{i,j}\frac{e^2}{4\pi\boldsymbol{\epsilon}|r_i-rj|}\Big]\boldsymbol{\psi}(r_1r_2.....r_n)\\&=E\boldsymbol{\psi}(r_1r_2.....r_n)\end{aligned} \tag{2.3}$$

In Eq.(2.3) $R_{l\boldsymbol{\alpha}}$ represents location of ions and $R_{l\boldsymbol{\alpha}} = R_l + \boldsymbol{\tau_\alpha}$; R_l is lattice vector and $\boldsymbol{\tau_\alpha}$ represents location of ion in the unit cell. m_o is the free electron mass. The third term on LHS of Eq.(2.3) corresponds to the energy due to electron electron repulsion. Using Hartree's [20] and mean field approximation one can approximate the effect of multiple electrons into an average field. Within this approximation system hamiltonian becomes $H_{el} = H_1 + H_2 + H_3 + \cdots\cdot H_n$ leading to the corresponding wavefunctions being $\boldsymbol{\psi}(r_1r_2\cdots\cdot r_n) = \boldsymbol{\psi}(r_1)\boldsymbol{\psi}(r_2)\boldsymbol{\psi}(r_3)\cdots\cdot\boldsymbol{\psi}(r_n)$. Next invoking the slater determinant [21] representation of the wave-function we can write the Hartree fock equation as

$$\begin{aligned}&\Big[\sum_{\boldsymbol{i}}\frac{p_i^2}{2m_o}+\sum_{\boldsymbol{i,j,l}}V_{\boldsymbol{\alpha}}(r_i-R_{l\boldsymbol{\alpha}})+\sum_{\boldsymbol{j\neq k}}\frac{e^2}{4\pi\boldsymbol{\epsilon}}\int\frac{\boldsymbol{\psi_j^*}(r')\boldsymbol{\psi_j}(r')}{|r-r'|}dr'\Big]\boldsymbol{\psi_i}(r)\\&-\sum_{\boldsymbol{j\neq k}}\frac{e^2}{4\boldsymbol{\pi}\epsilon_o}\boldsymbol{\psi_j}(r)\int\frac{\boldsymbol{\psi_j^*}(r')\boldsymbol{\psi_j}(r')}{|r-r'|}dr'=w_i\boldsymbol{\psi_i}(r)\end{aligned}\tag{2.4}$$

The last term on LHS of Eq.(2.4) is known as exchange energy and arises due to anti-symmetric nature of [22] spatial wave function. This causes electrons to repel each other so that they do not occupy the same state thus lowering the Coulomb repulsion. Exchange correlation energy becomes dominant for strongly correlated materials such as transition metal oxide [23]. For other materials where the exchange energy effects are not dominant one can still consider the mean field approximation to solve the Schrodinger equation. For the case of UTB SOI devices, using Si as a channel material, the mean field approximation works well. Thus, for bulk Si the Schrodinger equation takes the following form:

$$\Big[\frac{-\hbar^2}{2m_0}\nabla^2+V^{(lat)}(r)\Big]\boldsymbol{\psi}(r)=w_i\boldsymbol{\psi}(r)\tag{2.5}$$

The $V^{(lat)}$ term in Eq. (2.5) includes the ionic potential plus the screened potential due to other electrons in the system thereby representing the mean field experienced by the valence electrons in the semiconductor. We obtain band-structure by solving the Eq. (2.5). For solution purposes we can treat the above equation as eigenvalue problem for the energy values less than the confining potential determined by the device contacts. There are two ways to solve the problem :

1. **Tight binding method**: This method solves the eigenvalue problem in real space by considering the interaction of neighboring atoms in terms of coupling constants. It assumes that the valence electrons are tightly bound to the nucleus.

2. **Empirical Pseudo potential method (EPM)** : This method converts the eigenvalue problem in fourier space if the lattice potential in the crystal is periodic. It assumes that the valence electrons are loosely bound to the nucleus.

2.3 Introduction: EPM

Periodicity of the crystal potential, as depicted in the diagram Fig.(2.1) allows us to use the fourier expansion of the potential. Periodic potential leads to periodic wave functions. According to the Bloch theorem electron wave function can be written as a product of plane wave function and cell periodic part, namely $\boldsymbol{\psi_{nk}}(r) = exp(ikr)u_{nk}(r)$, where u_{nk} is cell periodic function. $u_{nk}(r) = u_{nk}(r + R)$ where R is lattice vector. Since Bloch function is periodic it can expressed as sum of its fourier components. $u_{nk}(r) = \sum_{\boldsymbol{j}} A(G_j)exp(iGr)$ and $\boldsymbol{\psi_{nk}}(r) = exp(ikr)\sum_{\boldsymbol{j}} A(G_j)exp(iGr)$. Earlier method to solve the schrodinger equation Eq. (2.5) involved use of plane waves and treated the periodic crystal potential as perturbation [24]. Using this approach one would require very large number of plane waves to correctly represent the valence electrons since many high frequency components would be required to depict the crystal potential towards the nucleus. This makes the scale of problem very large to solve. A way to get around this problem is to use Orthogonalized plane waves as eigenfunctions representing electron wave functions. If we consider the orthogonal basis set as follows we can greatly reduce the scale of problem [25].

$$\left|\boldsymbol{\phi^{OPW}_{k+K}}\right\rangle = |k + K\rangle - \sum_{\boldsymbol{c}} \langle \boldsymbol{\phi_c} | k + K\rangle \, |\boldsymbol{\phi_c}\rangle \tag{2.6}$$

In Eq. (2.6) $\boldsymbol{\phi_c}$ are the core atomic potentials. k represents the reduced zone k vector and K represents the reciprocal lattice vector.The orthogonalized plane waves also satisfy Eq.(2.5). This property is used to get next set of equations.

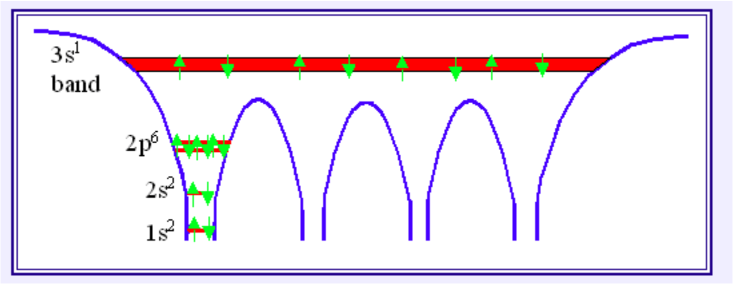

Figure 2.1: Periodic Crystal Potential

Fig. Courtesy @ [26]

$$\left[\frac{-\hbar^2}{2m_0}\nabla^2 + V^{(lat)}(r)\right][|k+K\rangle - \sum_{\boldsymbol{c}} \langle \boldsymbol{\phi_c}|k+K\rangle |\boldsymbol{\phi_c}\rangle] = w_i[|k+K\rangle - \sum_{\boldsymbol{c}} \langle \boldsymbol{\phi_c}|k+K\rangle |\boldsymbol{\phi_c}\rangle]$$

$$\left[\frac{-\hbar^2}{2m_0}\nabla^2 + V^{(lat)}(r)\right]|k+K\rangle - \left[\frac{-\hbar^2}{2m_0}\nabla^2 + V^{(lat)}(r)\right]\sum_{\boldsymbol{c}} \langle \boldsymbol{\phi_c}|k+K\rangle |\boldsymbol{\phi_c}\rangle$$

$$= w_i|k+K\rangle - w_i\sum_{\boldsymbol{c}} \langle \boldsymbol{\phi_c}|k+K\rangle |\boldsymbol{\phi_c}\rangle$$

Thus

$$\left[\frac{-\hbar^2}{2m_0}\nabla^2 + V^{(lat)}(r)\right]|k+K\rangle - E_c\sum_{\boldsymbol{c}} \langle \boldsymbol{\phi_c}|k+K\rangle |\boldsymbol{\phi_c}\rangle$$

$$= w_i|k+K\rangle - w_i\sum_{\boldsymbol{c}} \langle \boldsymbol{\phi_c}|k+K\rangle |\boldsymbol{\phi_c}\rangle$$

$Where\ E_c\ are\ the\ core\ atomic\ levels\ \therefore$

$$\left[\frac{-\hbar^2}{2m_0}\nabla^2 + V^{lat}(r)\right]|k+K\rangle + \sum_{\boldsymbol{c}}(w_i - E_c)|\boldsymbol{\phi_c}\rangle\langle \boldsymbol{\phi_c}|k+K\rangle = w_i|k+K\rangle \tag{2.7}$$

Thus the schrodinger equation takes the following form:

$$\left[\frac{-\hbar^2}{2m_0}\nabla^2 + V^{lat}_{pp}(r)\right]|k+K\rangle = w_i|k+K\rangle \tag{2.8a}$$

$$where\ :\ \ V^{lat}_{pp}(r) = V^{lat}(r) - \sum_{\boldsymbol{c}}(w_i - E_c)|\boldsymbol{\phi_c}\rangle\langle\boldsymbol{\phi_c}| \tag{2.8b}$$

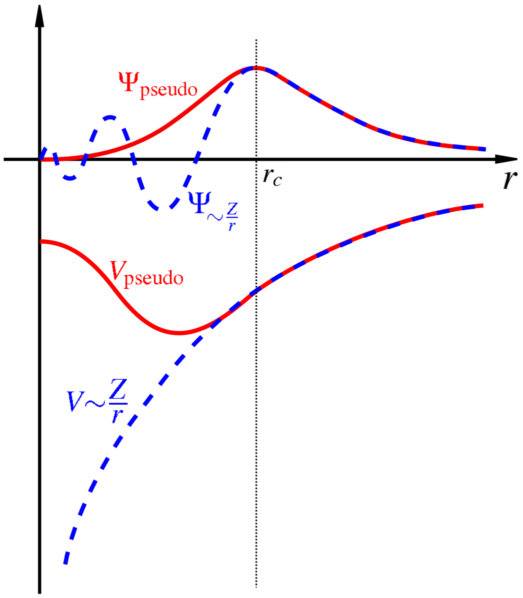

Figure 2.2: Atomic Pseudopotential

Fig. Courtesy @ [27]

Fig.(2.2) represents the pseudopotential, $V_{pp}^{(lat)}$ described in Eq.(2.8b). As we get closer and closer to the ionic potential the potential increases very rapidly but the pseudo-potential increases unto boundary of the core region and then decreases. There are many mathematical models to fit the pseudo potential curve. We adopted the model described by Zhang [1] These models are empirical in nature which implies that they are obtained by curve fitting to experimental values. For the ease of use in EPM, the pseudopotentials are usually plotted as function of the wave-vector q. Approximate expression for Si and H pseudopotentials are give in Eq.(2.9). The pseudopotential paramter values for Si and H are outlined in Table (2.1).

$$\begin{aligned} V^{Si}(q) =& \frac{b_1(q^2-b_2)}{b_3 e^{b_4 q^2}-1} \\ V^{H}(q) =& b_0 + b_1 q + b_2 q^2 + b_3 q^3 \; when \; q \leq 2 \\ =& \frac{b_{11}}{q} + \frac{b_{12}}{q^2} + \frac{b_{13}}{q^3} + \frac{b_{14}}{q^4} \; when \; q > 2 \end{aligned} \tag{2.9}$$

Note that $1Ry. = 13.60eV$ and $1a.u = \frac{1}{2}Ry$. Pseudo potential parameters are normalized to atomic volumes. For other materials one has to use appropriate empirical form for the lattice potential.

$Parameters(Si)$	b_1	b_2	b_3	b_4	$Ecutoff$
$Value(a.u.)$	0.2685	2.19104	2.05716	0.48716	9

b_0^H	b_1^H	b_2^H	b_3^H	b_{11}^H	b_{12}^H	b_{13}^H	b_{14}^H	$Ecutoff$
-0.1416	0.0098	0.06231	-0.01895	0.028	-0.3877	0.9692	1.022	16

Table 2.1: Local Pseudopotential Parameters for Si and H[1]

Pseudopotential parameters are normalized to Si and H atomic volumes

2.3.1 Schrodinger Equation in Fourier Space

To reiterate,

$$V^{lat}_{Si,pp}(r) = \sum_{\boldsymbol{j}} V(G_j) e^{iG_j r}$$

and the bloch function is,

$$\begin{aligned} \boldsymbol{\psi_{nk}}(r) &= e^{ikr} \sum_{\boldsymbol{i}} A_{nk}(G_i) e^{iG_i r} \\ &= \sum_{\boldsymbol{i}} A_{nk}(G_i) e^{i(k+G_i)r} = |k + G_i\rangle \end{aligned} \tag{2.10}$$

Substituting Eq.(2.10) in Eq.(2.8b) we get the fourier space representation of schrodinger equation.

$$\begin{aligned}
&\Big[\frac{-\hbar^2}{2m_0}\nabla^2 + \sum_{\boldsymbol{j}} V(G_j)e^{iG_jr}\Big]\sum_{\boldsymbol{i}} A_{nk}(G_i)e^{i(k+G_i)r} = w(k)\sum_{\boldsymbol{i}} A_{nk}(G_i)e^{i(k+G_i)r} \\
&\frac{-\hbar^2}{2m_0}\sum_{\boldsymbol{i}} |k+G_i|^2 A_{nk}(G_i)e^{i(k+G_i)r} + \sum_{\boldsymbol{j}}\sum_{i} V(G_j)A_{nk}(G_i)e^{i(k+G_i+G_j)r} \\
&= w(k)\sum_{\boldsymbol{i}} A_{nk}(G_i)e^{i(k+G_i)r}
\end{aligned} \tag{2.11}$$

Multiplying Eq.(2.11) with an orthogonal function $e^{-i(k+G_l)r}$ and integrating over volume of crystal introduces kronecker delta function:

$$\frac{-\hbar^2}{2m_0}\sum_{\boldsymbol{i}} |k+G_i|^2 A_{nk}(G_i)\delta_{G_i,G_l} + \sum_{\boldsymbol{j}}\sum_{i} V(G_j)A_{nk}(G_i)\delta_{G_j,G_l-G_i}$$

Then

$$\begin{aligned}
&= w(k)\sum_{\boldsymbol{i}} A_{nk}(G_i)\delta_{G_i.G_l} \\
&\frac{-\hbar^2}{2me}|k+G_l|^2 A_{nk}(G_l) + \sum_{\boldsymbol{i}} V(G_l-G_i)A_{nk}(G_i) = w(k)A_{nk}(G_l) \\
&\frac{-\hbar^2}{2me}|k+G_l|^2 \langle G_l|G_l\rangle\,|k+G_l\rangle + \sum_{\boldsymbol{i}} \langle G_i|\,V\,|G_l\rangle\,|k+G_l\rangle = w(k)\,\langle G_l|G_l\rangle\,|k+G_l\rangle
\end{aligned} \tag{2.12}$$

Eq.(2.12) can be represented as a eigenvalue problem with the first term representing the elements along the diagonal and the matrix elements corresponding to the pseudopotential are off diagonal. The matrix elements of the eigenvalue equation are are represented as $H_{i,j} = \frac{-\hbar^2}{2me}|k+G_i|^2\delta_{i,j} + \langle G_i|\,V\,|G_j\rangle$. Eq.(2.13) describes the computation of pseudo potential terms. The size of hamiltonian matrix is determined by the cut-off energy for individual atoms. The equation $\frac{-\hbar^2}{2me}|G|^2 \leq$Ecutoff determines the number of G-vectors required to obtain accurate band-structure plots.

The calculation of pseudopotential terms $\langle G_i | V | G_j \rangle$ is outlined here:

$$
\begin{aligned}
& V^{lat}(r) = \sum_{\boldsymbol{l},\boldsymbol{\alpha}} V^{\boldsymbol{\alpha}}(r - R_l - \tau_{\boldsymbol{\alpha}}) \\
& \quad \textit{where } \tau_{\boldsymbol{\alpha}} \textit{ represents position of atoms in the unit cell} \\
\langle G_i | V | G_j \rangle &= \frac{1}{\boldsymbol{\Omega}} \sum_{\boldsymbol{l},\boldsymbol{\alpha}} \int_{\boldsymbol{\Omega}} e^{-i(G_j - G_i)r} \sum_{\boldsymbol{l},\boldsymbol{\alpha}} V^{\boldsymbol{\alpha}}(r - R_l - \tau_{\boldsymbol{\alpha}}) dr \\
& \quad \textit{where } \boldsymbol{\Omega} \textit{ represents volume of crystal} \\
&= \frac{1}{\boldsymbol{\Omega}} \sum_{\boldsymbol{l},\boldsymbol{\alpha}} e^{-i(G_j - G_i)R_l} \int_{\boldsymbol{\Omega}} \sum_{\boldsymbol{l},\boldsymbol{\alpha}} V^{\boldsymbol{\alpha}}(r - R_l - \tau_{\boldsymbol{\alpha}}) e^{-i(G_j - G_i)(r - R_l)} dr \\
& \text{Using } r^{'} = r - R_l - \tau_{\boldsymbol{\alpha}} \\
\therefore \langle G_i | V | G_j \rangle &= \frac{1}{\boldsymbol{\Omega}} \sum_{\boldsymbol{l},\boldsymbol{\alpha}} e^{-i(G_j - G_i)R_l} \int_{\boldsymbol{\Omega}} \sum_{\boldsymbol{l},\boldsymbol{\alpha}} V^{\boldsymbol{\alpha}}(r^{'}) e^{-i(G_j - G_i)(r^{'} + \tau_{\boldsymbol{\alpha}})} dr^{'} \\
&= \sum_{\boldsymbol{\alpha}} e^{-i(G_j - G_i)\tau_{\boldsymbol{\alpha}}} \frac{1}{N_{cell}\boldsymbol{\Omega_c}} \sum_{\boldsymbol{l}} e^{-i(G_j - G_i)R_l} \int_{\boldsymbol{\Omega}} V^{\boldsymbol{\alpha}}(r^{'}) e^{-i(G_j - G_i)r^{'}} dr^{'} \\
&= \sum_{\boldsymbol{\alpha}} e^{-i(G_j - G_i)\tau_{\boldsymbol{\alpha}}} \frac{1}{N_{cell}\boldsymbol{\Omega_c}} N_{cell} \int_{\boldsymbol{\Omega}} V^{\boldsymbol{\alpha}}(r^{'}) e^{-i(G_j - G_i)r^{'}} dr^{'} \\
&= \sum_{\boldsymbol{\alpha}} e^{-i(G_j - G_i)\tau_{\boldsymbol{\alpha}}} \frac{1}{\boldsymbol{\Omega_c}} \int_{\boldsymbol{\Omega}} V^{\boldsymbol{\alpha}}(r^{'}) e^{-i(G_j - G_i)r^{'}} dr^{'} \\
& \because \text{the ionic pseudo potential fall off as } 1/r^2 \text{ one finally has} \\
& \int_{\boldsymbol{\Omega}} V^{\boldsymbol{\alpha}}(r^{'}) e^{-i(G_j - G_i)r^{'}} dr^{'} \approx \int_{\boldsymbol{\Omega_c}} V^{\boldsymbol{\alpha}}(r^{'}) e^{-i(G_j - G_i)r^{'}} dr^{'} \\
& \approx \sum_{\boldsymbol{\alpha}} e^{-i(G_j - G_i)\tau_{\boldsymbol{\alpha}}} \frac{1}{\boldsymbol{\Omega_c}} \int_{\boldsymbol{\Omega_c}} V^{\boldsymbol{\alpha}}(r^{'}) e^{-i(G_j - G_i)r^{'}} dr^{'}
\end{aligned}
\tag{2.13}
$$

2.4 Band-Structure of Thin Film Structures: Supercell Approach

As discussed in the introduction chapter FDSOI are successors for Moore's law and UTB SOI, which are FDSOI with very thin silicon channel are potential solutions to CMOS scaling. In this section it will be described how existing EPM technique is utilized to calculate the electronic properties of these thin film devices. The main difference between thin film and bulk devices is that bulk devices have periodicity in all the three spatial dimensions whereas thin film devices have periodicity in two dimensions and confinement in the third dimension. This confinement has important implications on the band-structure of thin films [28, 29].

To treat the confinement holistically we need to compute full band structure and to be able to do that we need to use the concept of supercells. Supercell is a unit cell consisting of least total number of atoms required to generate the whole structure using translation operation [30]. For the bulk band-structure case we usually have periodicity in all three directions. Hence the supercell is small in size implying there are very few atoms per supercell and this cell when translated in three dimensions gives us the complete crystal.

Due to the limited thickness of the silicon channel in UTB SOI devices there is confinement in the direction of channel thickness .Thus to study the electronic properties of confined devices we need to define a supercell long enough to accommodate the entire channel thickness along with the vacuum separation from the adjacent supercell. Thus supercell is nothing but extended unit cell in the confinement direction with larger number of atoms than in bulk primitive cell.The number of vacuum layers padded at both ends of the device are sufficiently long to avoid any coupling effects between the thin films in two adjacent super cells [32]. Fig. (2.4) represents the

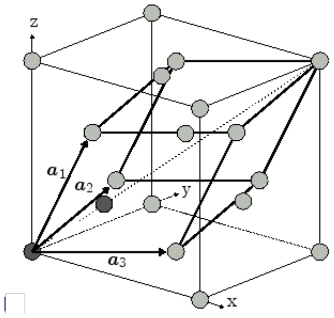

Figure 2.3: Crystal Structure of Silicon

FCC Lattice with two atoms per basis site. a_1, a_2, a_3 represent the primitive lattice vectors for the FCC lattice. Two atoms at the basis site form the Supercell.[31]

unit cell used for studying the electronic properties of thin film SOI devices. The idea of supercells can be very well extended to study the properties of devices like Si nanowires where the confinement expands in two spatial directions.

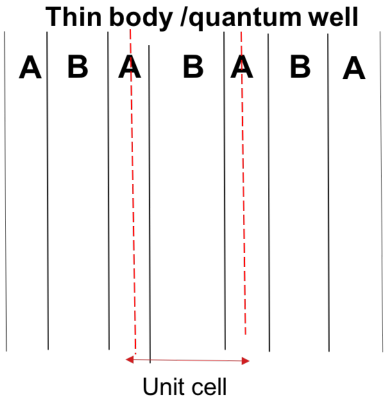

Figure 2.4: Unit Cell Representation for Thin Film Devices

Region B represents the thin film and Region A represents the vacuum padding used to form non coupled supercell.[32]

2.5 Thin Si Layers

In this section we study how the concept of supercell is applied to study the properties of thin film devices. Thin film devices differ from MOSFET in a way that they have structural confinement in addition to the electrical confinement. As discussed in the beginning of the chapter, EME (Effective Mass equation) is the most widely invoked method to study the electronic properties of MOSFET. But in UTB SOI devices, due to quantum confinement the energy levels in the device are higher as compared to bulk. This makes the EME equation unreliable since as we go higher in energy non-parabolic nature of bands become dominant. Thus we adopt empirical pseudo potential (EPM) method for band structure calculation.Confinement effects were studied for two crystallographic orientations namely [100] and [110] using EPM. Due to confinement in the z direction, the wave-function is no longer a plane wave in the z-direction as in case of bulk. Instead it assumes the following form $\boldsymbol{\phi_{n,k_\parallel}} = e^{ik_\parallel r_\parallel}\boldsymbol{\lambda_z}$ where $k_\parallel$ represents the wave-vector in the plane perpendicular to the direction of confinement and $\boldsymbol{\lambda_z}$ represents the wavefunction in the confinement direction. n is the band index corresponding to the sub-bands resulting from quantum confinement. Solution to Eq. (2.14) will give us the required band structure.

$$\sum_{\boldsymbol{G'}}\Big[\frac{\hbar^2}{2m_e}|k+G|^2\delta_{G,G'} + V^{lat}_{G-G'}\Big]\boldsymbol{\lambda^{n}_{G,k_\parallel}} = E_n(k_\parallel)\boldsymbol{\lambda^{n}_{G,k_\parallel}} \tag{2.14}$$

Thus, the eigen energies in Eq.(2.14) are function of in plane wave-vector $k_\parallel$.

2.5.1 [100] Si Layers

The first step in calculating the band structure is defining the unit cell and the placement of the atoms in the unit cell. The unit cell helps us to calculate the structure factor which eventually appears in the pseudo potential term in the Hamiltonian in Eq. (2.14). The supercell for [100] oriented Silicon layers are constructed by projecting the bulk lattice vectors on x-y plane. Fig. (2.5a) represents the top view of the unreconstructed Si(100) surface with two dangling bonds. Fig. (2.5b) represents the top view of dimerized Si(100) surface with one dangling bond. Fig. (2.5c) represents the hydrogen terminated Si(100) surface. The surface atoms are depicted in black and the sub-surface atoms are depicted in gray [33]. For the present work the Si surface considered for (100) thin films is unreconstructed with two dangling bonds. The unit cell (supercell) vectors for [100] thin film silicon in rectangular co-ordinate

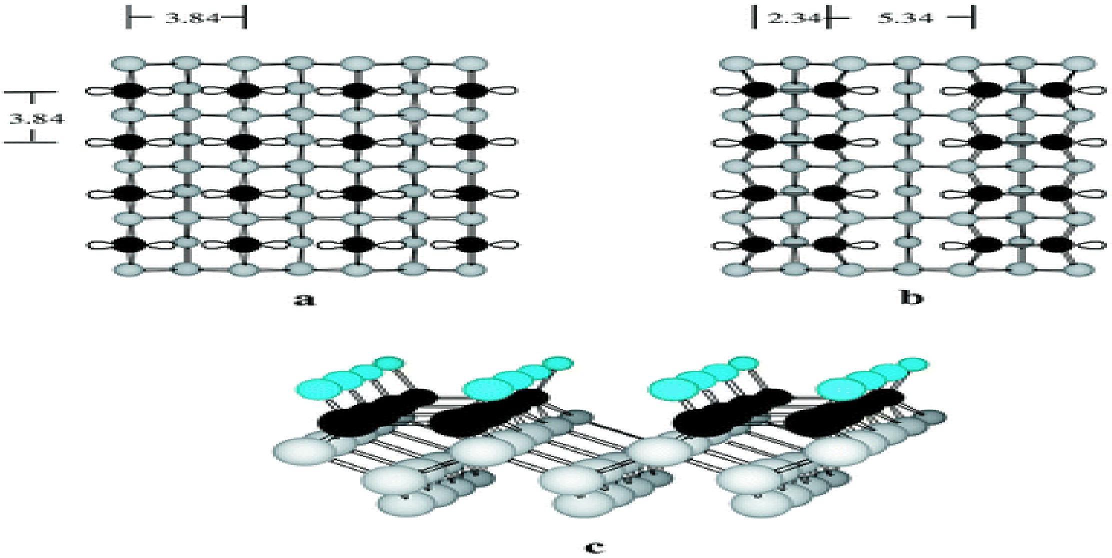

Figure 2.5: Atomic Arrangement in Thin Film Silicon: [100] Crystallographic Orientaion

Figure Courtsey @[33]

system are:

- $a1 = a_0/2\Big[1,1,0\Big]$
- $a2 = a_0/2\Big[-1,1,0\Big]$
- $a3 = a_0\Big[0,0,N_{si}+N_v\Big]$

N_{si} denotes the number of Silicon layers in the unit cell and N_v denotes the number of vacuum cells used for isolation. Let $N = N_{si} + N_v$ denote the total number of layers in the supercell. N_{si} determines the channel thickness. Si atoms are placed in the supercell spanned by the vectors a_1, a_2, a_3 starting with four atoms in the first layer with the co-ordinates [32]:

- $\boldsymbol{\tau_1} = a_0/4\Big[0,0,1/2\Big] + N_v a_0/2\Big[0,0,1\Big]$
- $\boldsymbol{\tau_2} = a_0/4\Big[1,1,3/2\Big] + N_v a_0/2\Big[0,0,1\Big]$
- $\boldsymbol{\tau_2} = a_0/4\Big[0,2,5/2\Big] + N_v a_0/2\Big[0,0,1\Big]$
- $\boldsymbol{\tau_2} = a_0/4\Big[-1,1,7/2\Big] + N_v a_0/2\Big[0,0,1\Big]$

The remaining Si atoms in the supercell(unit cell) are placed at the following co-ordinates [32] where $j = 0 : N_{si} - 1$:

- $\boldsymbol{\tau_{4j+1}} = \boldsymbol{\tau_1} + ja_0\Big[0,0,1\Big]$
- $\boldsymbol{\tau_{4j+2}} = \boldsymbol{\tau_2} + ja_0\Big[0,0,1\Big]$
- $\boldsymbol{\tau_{4j+3}} = \boldsymbol{\tau_3} + ja_0\Big[0,0,1\Big]$
- $\boldsymbol{\tau_{4j+4}} = \boldsymbol{\tau_4} + ja_0\Big[0,0,1\Big]$

At the surface of these free Si thin films there will be unsatisfied dangling sp^3 bonds due to missing atoms. These dangling bonds lead to unwanted surface states lying in the band-gap. Hence, in order to avoid the surface states, the dangling bonds are terminated by hydrogen.The hydrogen pseudopotential parameters that avoid the formation of surface states are listed in table[2.1]. The hydrogen atoms are positioned in the supercell at Si dangling bond site but with bond length corresponding to $0.158a_o$ where a_0 is Si lattice constant. The bond length is determined empirically. Co-ordinates corresponding to hydrogen atom in the supercell are :

- $\boldsymbol{\tau_{H,1}} = \boldsymbol{\tau_1} + 0.158a_0\Big[-1, 1, -1\Big]$
- $\boldsymbol{\tau_{H,2}} = \boldsymbol{\tau_1} + 0.158a_0\Big[1, -1, -1\Big]$
- $\boldsymbol{\tau_{H,3}} = \boldsymbol{\tau_{4N_{si}}} + 0.158a_0\Big[-1, 1, 1\Big]$
- $\boldsymbol{\tau_{H,4}} = \boldsymbol{\tau_{4N_{si}}} + 0.158a_0\Big[1, -1, 1\Big]$

Fig.(2.6) represents the 2D Brillouin zone (BZ) corresponding to [100] Si films over which electronic properties are calculated. In fig.(2.6) T$\Rightarrow [0, 0, 0]$, $\overline{X} \Rightarrow [0, 1/\sqrt{2}, 0]$ and $\overline{H} \Rightarrow [1/\sqrt{2}, 1/\sqrt{2}, 0]$ are the high symmetry points in the first brillouin zone. The area marked by the dashed boundaries represents the irreducible triangle of brillouin zone. Since the entire first BZ can be formed from the irreducible triangle it is sufficient to calculate the electronic properties of the device along in the irreducible region.

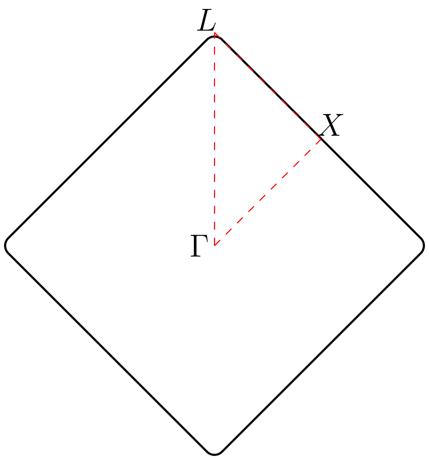

(100) Brillouin zone

Figure 2.6: First Brillouin Zone for [100] Thin Film Si

Fig. Courtesy @ [32]

2.5.2 [110] Si Layers

[110] oriented silicon films have shown better performance over [100] oriented silicon films for p-MOSFET [13]. Thus it is beneficial to study the properties of UTB DG SOI MOSFET with [110] oriented silicon channel.The unit cell lattice vectors for [110] si layers are defined as[32]:

- $a1 = a_0/\sqrt{2}\Big[1, 0, 0\Big]$
- $a2 = a_0/2\Big[0, 1, 0\Big]$
- $a3 = a_0/\sqrt{2}\Big[0, 0, N_{si} + N_v\Big]$

$N_{si} + N_v$ represent the total length of the supercell. Thus silicon atoms are placed in this supercell spanned by three lattice vectors beginning with four atoms in one layer. The coordinates [32] of silicon atom in the first non vacuum layer are:

- $\boldsymbol{\tau_1} = a_0/4\Big[0,0,0\Big] + N_v a_0/\sqrt{2}\Big[0,0,1\Big]$
- $\boldsymbol{\tau_2} = a_0/4\Big[0,1,2/\sqrt{2}\Big] + N_v a_0/\sqrt{2}\Big[0,0,1\Big]$
- $\boldsymbol{\tau_2} = a_0/2\Big[1/\sqrt{2},1,1/\sqrt{2}\Big] + N_v a_0/\sqrt{2}\Big[0,0,1\Big]$
- $\boldsymbol{\tau_2} = a_0/4\Big[2/\sqrt{2},3,0\Big] + N_v a_0/\sqrt{2}\Big[0,0,1\Big]$

The remaining 4N-1 atoms are placed at the following locations: $j = 0 : N_{si} - 1$:

- $\boldsymbol{\tau_{4j+1}} = \boldsymbol{\tau_1} + ja_0\sqrt{2}\Big[0,0,1\Big]$
- $\boldsymbol{\tau_{4j+2}} = \boldsymbol{\tau_2} + ja_0\sqrt{2}\Big[0,0,1\Big]$
- $\boldsymbol{\tau_{4j+3}} = \boldsymbol{\tau_3} + ja_0\sqrt{2}\Big[0,0,1\Big]$
- $\boldsymbol{\tau_{4j+4}} = \boldsymbol{\tau_4} + ja_0\sqrt{2}\Big[0,0,1\Big]$

As for [100] Si films the dangling bonds here are terminated by hydrogen.The coordinates of hydrogen atoms are:

- $\boldsymbol{\tau_{H,1}} = \boldsymbol{\tau_1} + 0.158a_0\Big[0,1,-\sqrt{2}\Big]$
- $\boldsymbol{\tau_{H,2}} = \boldsymbol{\tau_1} + 0.158a_0\Big[0,-1,-\sqrt{2}\Big]$
- $\boldsymbol{\tau_{H,3}} = \boldsymbol{\tau_{4N_{si}-2}} + 0.158a_0\Big[0,-1,\sqrt{2}\Big]$
- $\boldsymbol{\tau_{H,4}} = \boldsymbol{\tau_{4N_{si}-1}} + 0.158a_0\Big[0,1,\sqrt{2}\Big]$

In fig.(2.7) T$\Rightarrow$ $[0,0,0]$, X$\Rightarrow$ $[1/\sqrt{2},0,0]$, X$^{'}$ $\Rightarrow$ $[0,1/2,0]$ and M $\Rightarrow$ $[1/\sqrt{2},1/2,0]$ are the high symmetry points in the first brillouin zone. As in fig.(2.6) the dashed region marks the irreducible portion of the first BZ.

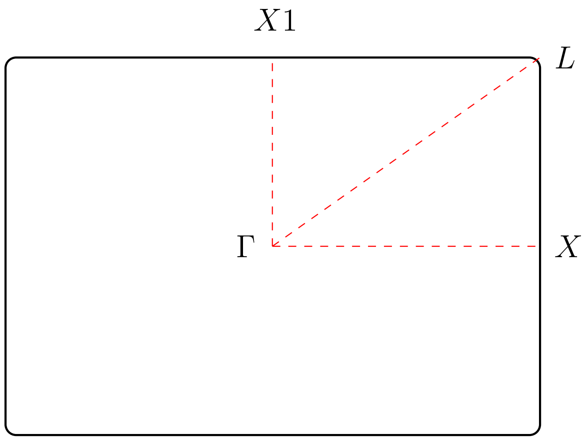

(110) Brillouin zone

Figure 2.7: First Brillouin Zone for [110] Thin Film Si.

Fig. Courtesy @ [32]

2.6 Bandstructure Results

One of the important effects we observe due to the structural confinement on bandstructure is that thin Si layers become a direct band-gap material. Also the bandgap increases as the thickness of the device decreases. Transition of Si thin films from indirect to direct band-gap material is result of projecting the bulk 3D bulk bands onto 2D BZ. For bulk Si the top of valence band is already at the $\mathbf{\Gamma}$ symmetry point. Six conduction X valleys of Si are aligned along the device axes for [100] crystallographic orientation. In case of confinement in the z direction, the two X valleys aligned along the confinement are projected at the $\mathbf{\Gamma}$ point. If the remaining 4 X valleys are higher in energy than the valley projected at the $\mathbf{\Gamma}$ then the material becomes a direct bandgap. Fig.(2.8) shows that bandgap increases with decrease in thickness for [100] si

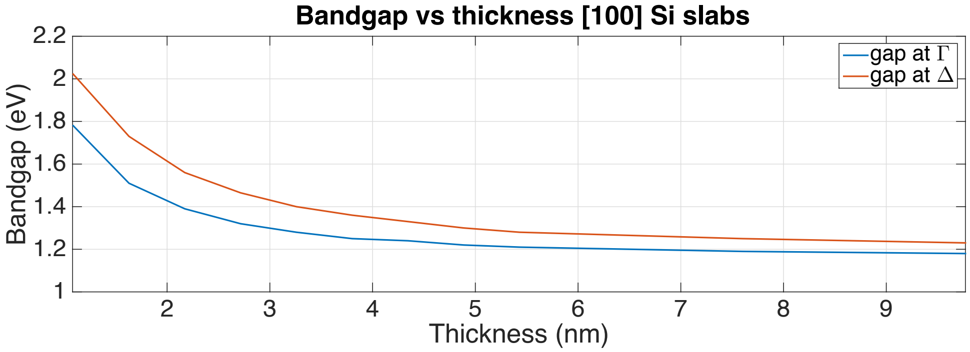

Figure 2.8: Variation of Bandgap With Film Thickness for [100] Si Slabs

thin films. According to EMT (Effective Mass Theory), the bands projected at the Γ point have higher effective mass m^* ($\approx 0.91m_0$ where m_0 is free electron mass) in the confined direction as compared to effective mass for remaining four X valleys ($\approx 0.19m_0$). The kinetic part of ground state energy of particle in a quantum well is inversely proportional to $1/m^*$. Thus bandgap widening due to reduced channel thickness is more pronounced for bands with lower effective mass. Hence, conduction bands at $\boldsymbol{\Delta}$ point show more bandgap widening as compared to that at Γ point. The trend depicted in Fig.(2.8)is in agreement with the EMT prediction. The bandgap depicted Fig.(2.9) is 1.78 eV and that in Fig.(2.10) is 1.19 eV.

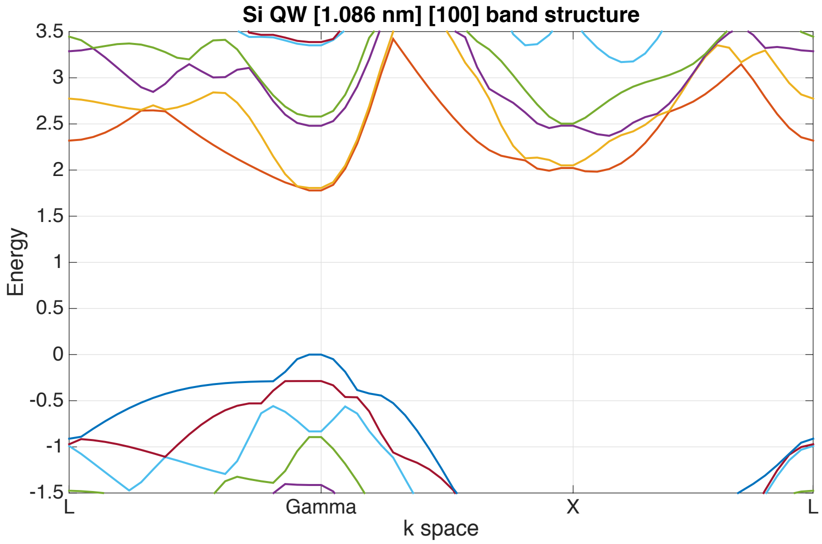

Figure 2.9: Band Structure of 1.086 Nm Thick and [100] Oriented Si Slab

Fig.(2.11) shows that for thicknesses greater than $3nm$ both [100] and [110] Si thin film layers have almost the same band-gap. For thicknesses below $1.15nm$ [110] Silicon films are direct band-gap materials whereas above $1.15nm$ it becomes indirect band-

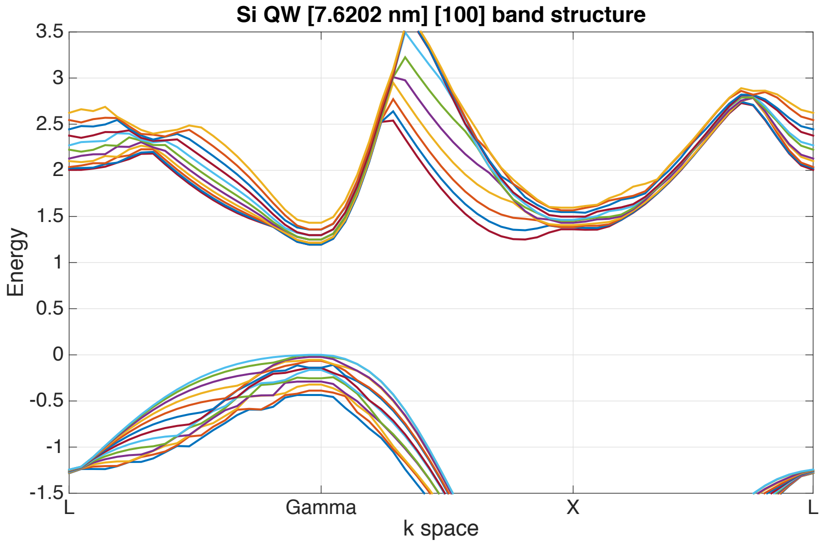

Figure 2.10: Band Structure of 7.62 Nm Thick and [100] Oriented Si Slab

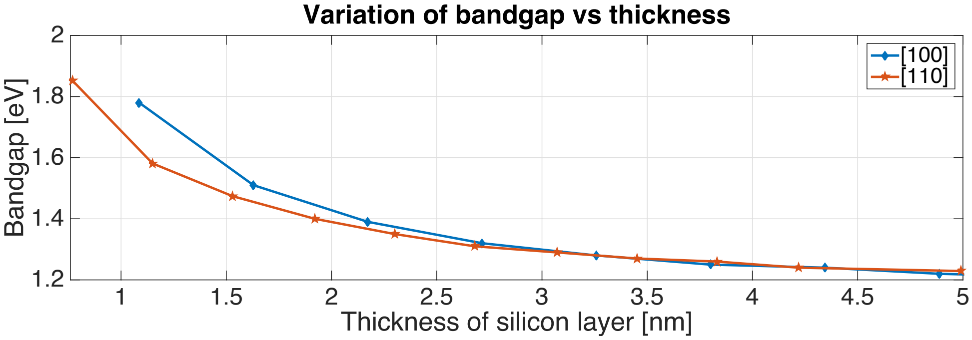

Figure 2.11: Variation of Bandgap With Silicon Film Thickness for [100] vs [110] Crystallographic Orientation

gap material. Also the increase in the band-gap due to reduction in film thickness is greater for [100] films than [110] Si films at the same thickness. Fig.(2.13) shows the direct band-gap nature at thickness of about 0.769 nm with a bandgap of 1.853 nm whereas Fig.(2.14) shows indirect band-gap nature at thickness of about 2.3 nm with band-gap of 1.35 nm. Fig.(2.12) shows that the band-structure calculations for thin Si films follow the same trend as the experimental data. Experimental data for bandgap variation with Si film thickness corresponds to the bandgap of Si in $Si{-}SiO_2$ quantum well structure. [34]. The difference in the experimental and simulated data can be

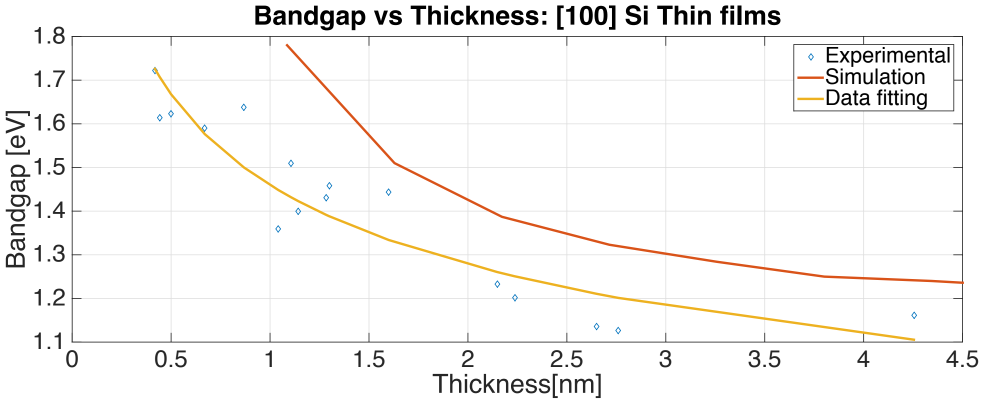

Figure 2.12: Comparison of the Bandgap Variation for Thin Si(100) Films With Experimental Results

attributed to the fact that for the thesis work we considered hydrogen terminated Si surface rather than termination with SiO_2 . Also the transition of Si into Sio_2 layers is over few atomic layers rather begin abrupt implying that there is no sharp barrier as assumed in case of padding Si layers with vacuum in supercell. The quadratic fit on the experimental data, helps us compare the experimental and simulated data very well.

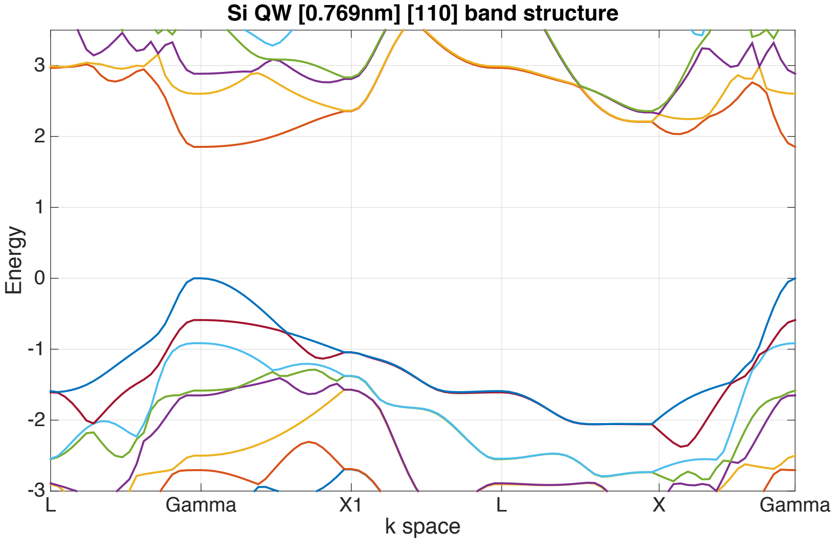

Figure 2.13: Band Structure of 0.77 Nm Thick [110] Oriented Si Slab

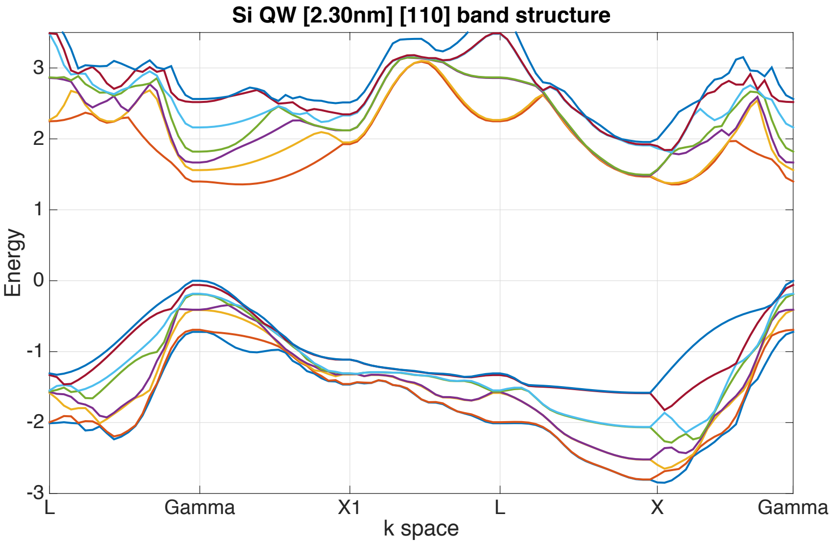

Figure 2.14: Band Structure of 2.3 Nm Thick [110] Oriented Si Slab

Chapter 3

ELECTRON AND HOLE CONCENTRATION

3.1 Density of States Calculation

Band-structure calculation gives us the idea about the available energy states that can be occupied by electrons and holes in solids. On the other hand, density of states(DOS), that is derived from the band-structure, gives us the number of available states that can be occupied by electrons and holes per unit volume and per unit energy at a given energy. DOS calculations are essential to determine the carrier concentration and energy distribution of carriers within the semiconductor. In semiconductors the motion of carrier can be in one, two or three spatial dimensions. Let N(E) represent the number of states per unit volume at particular energy and D(E) represent density of state as a function of energy(E). Then :

$$g(E) = \frac{dN}{dE}$$

$$g(E) = \frac{dN}{dk}\frac{dk}{dE} \tag{3.1}$$

where $\frac{dN}{dk}$ represents the density of states in k-space

For the case of thin Si slabs transport occurs in plane that is perpendicular to the direction of confinement. Hence, one needs to compute the density of states over the 2D Brillouin zone. We first ananlyze the DOS expression in effective mass regime and then extend the formalism to calculate the DOS directly from the band-structure. In Fig.(3.1) for every value of k_x, k_y and band index n there exist two states considering spin degeneracy. For effective mass approach the constant energy surfaces corresponding to E and E+dE turn out to be circular $\because E = \frac{\hbar^2 k^2}{2m^*}$. Thus we can find DOS in energy space by calculating the DOS in k-space. The wave-vectros for finite solids

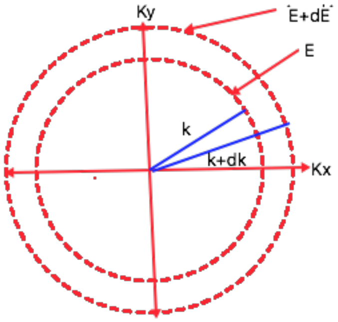

Figure 3.1: Area in 2D K-Space

are of the following form:

$$k_i = \frac{2\pi h}{L_i a_0}, \tag{3.2}$$

$$\text{where h} \in \mathbb{I} \text{ and } L_i a_0 \text{ is length of crystal in } i^{th} \text{ dimension.}$$

Thus the area of k-space containing single state is $a = \frac{4\pi^2}{\mathbf{\Omega}}$ where $\mathbf{\Omega}$ is area of cross-section. Hence, the number of states lying in the area dA of the k-space is

$$\begin{aligned}
&\frac{N}{A} = \frac{1}{\frac{4\pi^2}{\mathbf{\Omega}}} \\
&A = \pi k^2 \\
&\therefore N = \frac{\mathbf{\Omega}\pi k^2}{4\pi^2} \\
&\Rightarrow \frac{N}{\mathbf{\Omega}} = \frac{k^2}{4\pi} \\
&N^{'} = \frac{k^2}{4\pi} \\
&\text{where } N^{'} \text{ represents number of states per unit area} \\
&\text{at particular energy E}
\end{aligned} \tag{3.3}$$

Using Eq.(3.1) and Eq.(3.3) and taking into account spin degeneracy we can compute the density of states expression for 2D.

$$
\begin{aligned}
g(E) &= \frac{2\cdot 2k}{4\pi}\frac{dk}{dE}, \text{where} \\
g(E)dE &= \frac{kdk}{\pi}, \text{or} \\
g(E)dE &= \frac{2\cdot 2\pi kdk}{4\pi^2} \\
g(E)dE &= \frac{2\cdot d\mathbf{\Omega}}{4\pi^2}
\end{aligned}
\tag{3.4}
$$

where $d\mathbf{\Omega}$ represents the area between two equienergy contours.

To summarize :

$$
\begin{aligned}
g(E)dE &= \frac{2\cdot d\mathbf{\Omega}}{4\pi^2} \\
g(E)dE &= \frac{\int_{E=constant} dldk}{2\pi^2}
\end{aligned}
\tag{3.5}
$$

where dl is the length of equienergy contour and

dk is the distance in k-space between two equienergy contours.

Then :

$$g(E) = \frac{\int_{E=constant} dl}{2\pi^2\cdot\frac{dE}{dk}}$$

$$
\begin{aligned}
g(E) &= \frac{\int_{E=constant} dl}{2\pi^2\cdot|\nabla_k E|} \\
&= \frac{\sum_{\boldsymbol{j,n}} L(j,n)}{|\nabla_k E|}
\end{aligned}
\tag{3.6}
$$

In Eq. (3.6) L(j,n) is the length of the equienergy contour corresponding to energy E [32] intersecting the k-space grid point k_j having eigen energy $E_{j,n}$ and n is the band index. Eq.(3.6) describes the numerical density of states calculation for full band computations. The technique presented for density of states calculation is 2D extension of the Gilat Raubenheimer (GR) alogorithm used for 3D density of states calculation[36]. The implementation details of GR algorithm for 2D case are outlined in Appendix A.

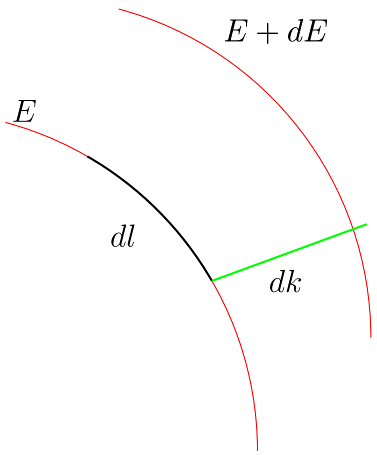

Figure 3.2: Density of State Derivation

Figure courtesy @ [35]

3.2 Energy Gradient Calculation

$$H\boldsymbol{\psi} = E\boldsymbol{\psi} \tag{3.7}$$

According to Eq.(3.6) for density of states calculation we need to compute:

- L(j,n)
- $|\nabla_k E|$

Computation of $L(j, n)$ is described in Appendix A. The following section discusses the calculation of gradient of energy with respect to wavevector k. Using Eq.(3.7), we can write eigenenergy E as

$$\begin{gathered} \langle\boldsymbol{\psi}| H |\boldsymbol{\psi}\rangle = E \\ \frac{\partial \langle\boldsymbol{\psi}| H |\boldsymbol{\psi}\rangle}{\partial k} = \frac{\partial E}{\partial k} \end{gathered} \tag{3.8}$$

Using the product rule for Eq.(3.8)

$$\left\langle \frac{\partial \boldsymbol{\psi}}{\partial k} \right| H \left|\boldsymbol{\psi}\right\rangle + \left\langle\boldsymbol{\psi}\right| \frac{\partial H}{\partial k} \left|\boldsymbol{\psi}\right\rangle + \left\langle\boldsymbol{\psi}\right| H \left| \frac{\partial \boldsymbol{\psi}}{\partial k} \right\rangle = \frac{\partial E}{\partial k} \tag{3.9}$$

$$\therefore \left\langle\boldsymbol{\psi}\right| \frac{\partial H}{\partial k} \left|\boldsymbol{\psi}\right\rangle = \frac{\partial E}{\partial k}$$

3.3 Full Band DOS: [100] and [110]

The density of states depicted in Fig.(3.3) deviates significantly from that expected by parabolic band approximation. Thus, it is necessary to adopt full band approach for band-structure calculations to get correct value of density of states. Once the density of states are obtained, we need to compute the electron and hole charge concentrations that will be fed into the Poisson solver for self-consistent solution.

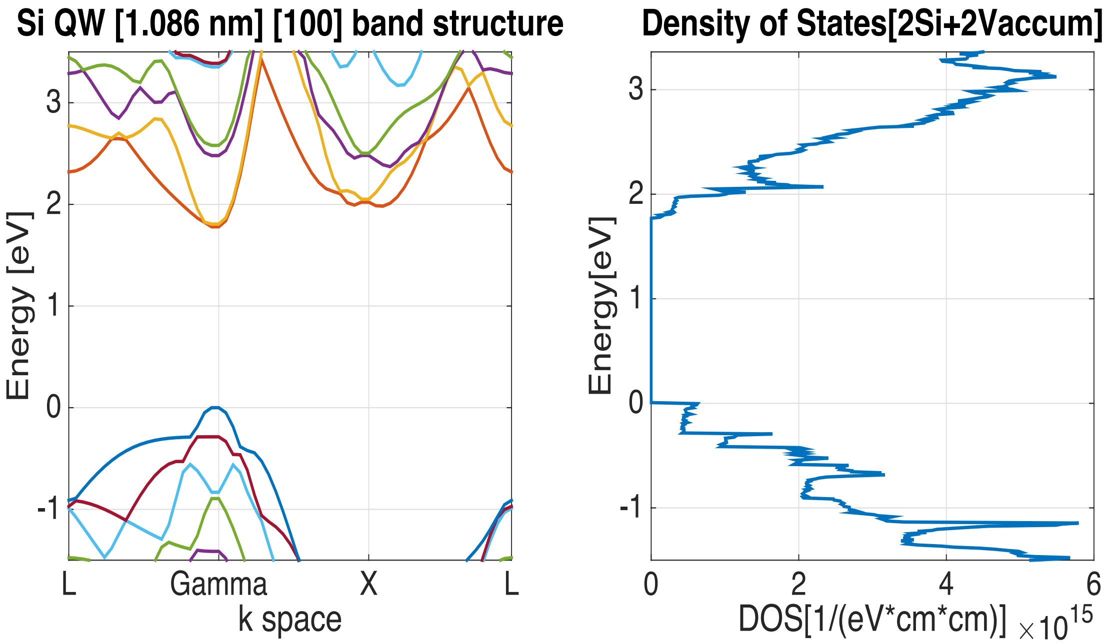

Figure 3.3: Density of States: [100] Oriented 1.08 nm Thick Si Film

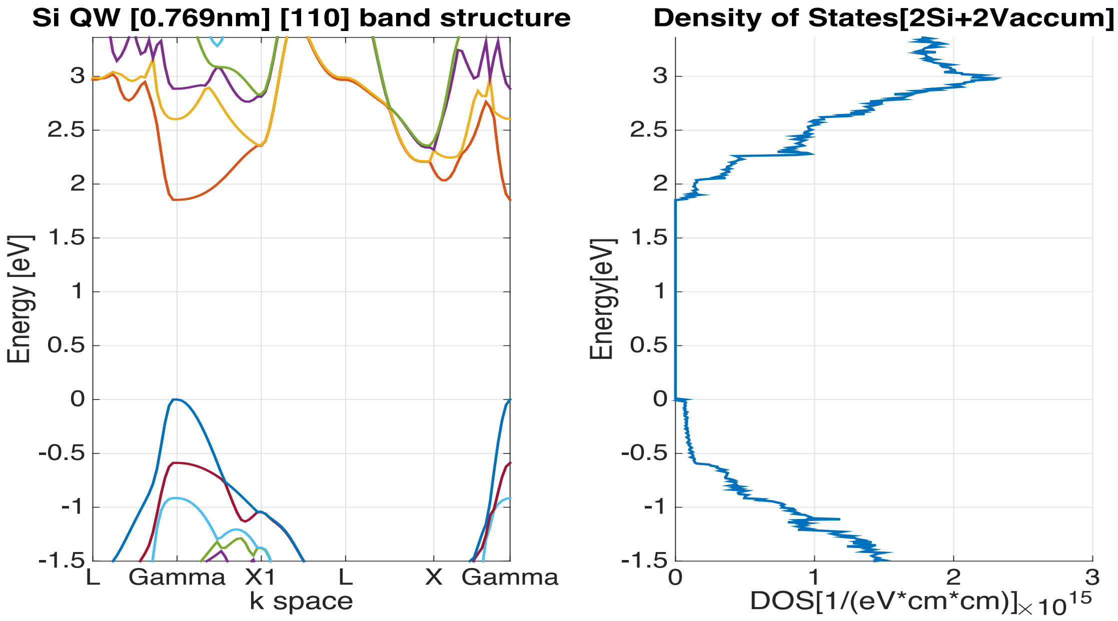

Figure 3.4: Density of State for [110] Oriented 0.769 nm Thick Si Film

3.4 Electron and Hole Concentration

Let $n(z), p(z)$ denote electron and hole concentrations per unit volume respectively. As we are studying equilibrium characteristics of DG SOI device we can assume that the carriers are at thermal equilibrium. Hence, electrons follow the Fermi dirac distribution. Fermi function is denoted by $f(E)$. As holes are nothing but absence of electrons hence, their distribution is governed by $(1 - f(E))$. The Fermi-Dirac statistics reads:

$$f(E) = \frac{1}{1 + e^{\frac{E-E_f}{k_bT}}} \tag{3.10}$$

Then :

$$\begin{aligned} n(z) &= \sum_{\boldsymbol{n}}\sum_{\boldsymbol{j}} f(E(j,n))D(E(j,n))|\boldsymbol{\psi_{j,n}(z)}|^2 \\ p(z) &= \sum_{\boldsymbol{n}}\sum_{\boldsymbol{j}} (1 - f(E(j,n)))D(E(j,n))|\boldsymbol{\psi_{j,n}(z)}|^2 \end{aligned} \tag{3.11}$$

In Eq.(3.11) the two summmations represent contributions to carrier concentration from all points in k-space (lying in the first BZ) denoted by j and all the sub-bands n. $|\boldsymbol{\psi_{j,n}(z)}|^2$ represents probability amplitude squared along the confined direction. Thus having determined density of states in this section, we next discuss the calculation of wavefunction which will help us determine $|\boldsymbol{\psi_{j,n}(z)}|^2$. Wavefunctions are the eigenvectors of the Hamiltonian H described in Eq.(3.7).

3.5 Electron Wavefunction

For electrons or holes in a periodic crystal where V_c is the crystal volume the electron wavefunctions are Bloch functions of the form:

$$\begin{aligned}\boldsymbol{\psi_{nk}}(r) &= \frac{1}{\sqrt{Vc}}\exp(\imath kr)u_{nk}(r)\\ \boldsymbol{\psi_{nk}}(r) &= \frac{1}{\sqrt{V_c}}exp(\imath kr)\sum_{\boldsymbol{j}} A_n(k+G_j)\exp(iG_j\cdot r)\end{aligned} \tag{3.12}$$

The second line in equation (3.12) represents the Fourier decomposition of the Bloch waves where k is the electron wave-vector and G_j are reciprocal lattice vectors. Subscript n represents the sub-band index. The fourier co-efficients $A_n(k+G_j)$ are the eigenvectors corresponding to the Hamiltonian described in Eq.(2.14). For simplicity we consider the wavefunctions to be independent of the in plane wave-vector k. Then

$$\therefore \boldsymbol{\psi_{n,k}}(r) = \boldsymbol{\psi_{n,k=0}}(r) \tag{3.13}$$

The ellectron wavefunction along the confined direction is $\boldsymbol{\psi_{n,k}}(z)$, where z is the confined direction.

$$\boldsymbol{\psi_{n,k}}(z) = \int_\Omega \boldsymbol{\psi_{n,k}}(r)dxdy \tag{3.14}$$

Ω represents unit cell area perpendicular to the direction of confinement.

Using Eq.(3.13), Eq.(3.12) and Eq.(3.14) we can express:

$$\begin{aligned}\boldsymbol{\psi_{n,k}}(z) &= \int_\Omega \frac{1}{\sqrt{V}_c}\sum_{\boldsymbol{j}} A_n(G_j)\exp(iG_j \cdot r)dxdy \\ = \frac{1}{\sqrt{V}_c}&\int_\Omega \sum_{\boldsymbol{j}} A_n(G_j)exp(iG_{j_z}z)\exp(iG_{j_x}x)exp(iG_{j_y}y)dxdy\end{aligned} \tag{3.15}$$

The unit cell for [100] silicon supercell is defined by the following lattice vectors [32]:

- $a_1 = a_0 \cdot [\frac{1}{\sqrt{2}}, 0, 0]$
- $a_2 = a_0 \cdot [0, \frac{1}{\sqrt{2}}, 0]$
- $a_3 = a_0 \cdot [0, 0, l]$
- $\boldsymbol{\Omega} = a_0^3 \cdot l/2$

$$\begin{aligned}&\text{Using physics notataion for kronecker delta} \\ &\because \frac{1}{\sqrt{l_x}}\int_{l_x} exp(iG_x x)dx = \delta(G_x) \\ &\text{Then} : \boldsymbol{\psi_{n,k}}(z) = \frac{\sqrt{\Omega}}{\sqrt{V}_c}\sum_{\boldsymbol{j}} A_n(G_j)exp(iG_{j_z}z)\delta(G_x)\delta(G_y) \\ &\boldsymbol{\psi_{n,k}}(z) = \frac{1}{\sqrt{l}_z}\sum_{\boldsymbol{j}} A_n(G_j)exp(iG_{j_z}z)\delta(G_\parallel)\end{aligned} \tag{3.16}$$

$$\therefore |\boldsymbol{\psi_{n,k}(z)}|^2 = \boldsymbol{\psi^*_{n,k}\psi_{n,k}} \tag{3.17}$$

3.6 Wavefunction Plots

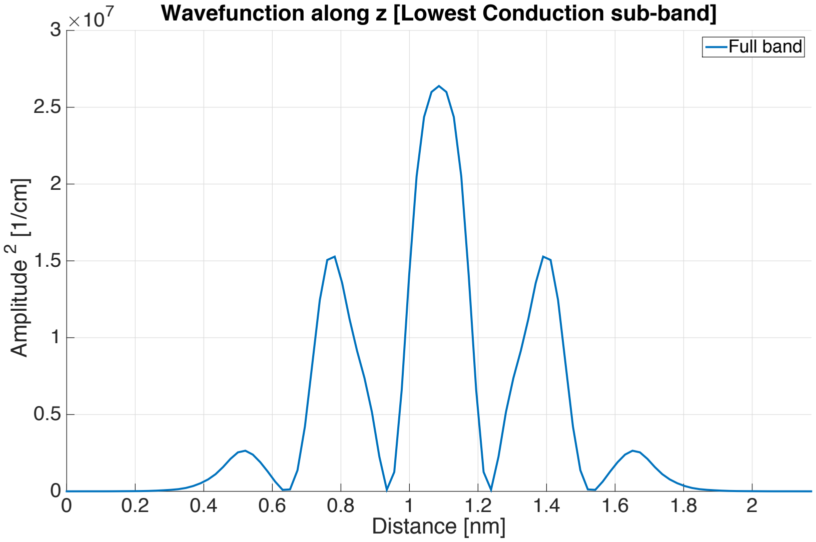

Figure 3.5: Lowest Conduction Sub-band: 1.08 nm [100] Si Film

Shown in Fig.(3.5), Fig.(3.6), Fig.(3.7), Fig.(3.8) and Fig.(3.9) are the wavefunction squared plots corresponding to the wavefunction in the confined direction for [100] and [110] wafer orientations. Thus we find that the envelope wavefunction related to lowest conduction sub-band wavefunction has no node in the channel whereas that related to second lowest conduction sub-band has single node in the channel as would be expected for wavefunctions in thin Si films (which can be approximated to Quantum well structure). The oscillations obtained in wavefunction squared result from the fact that bloch wavefunctions are the eigenfunctions of the full band calculations and are of the form: $\boldsymbol{\psi}(z) = sin(k_z z)u_{n,k_z}$ where $k_z = \frac{n\pi}{L_z}$.

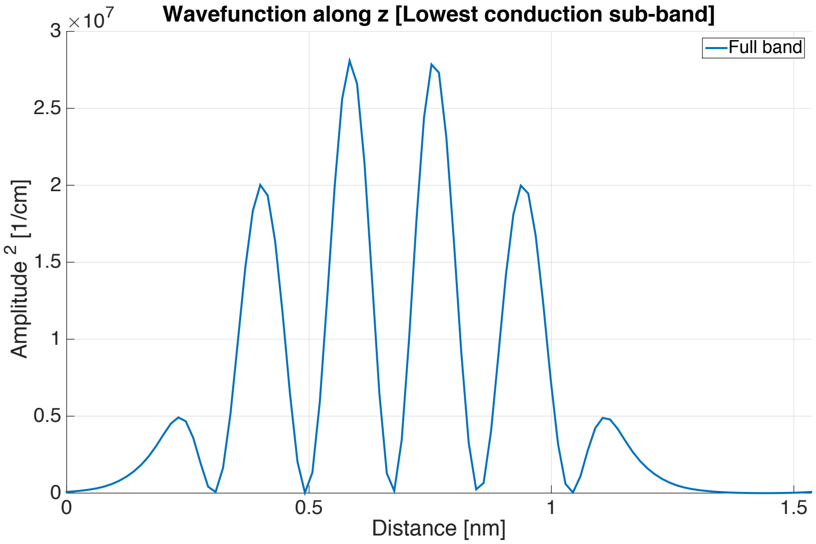

Figure 3.6: Lowest Conduction Sub-band: 0.769 nm [110] Si Film

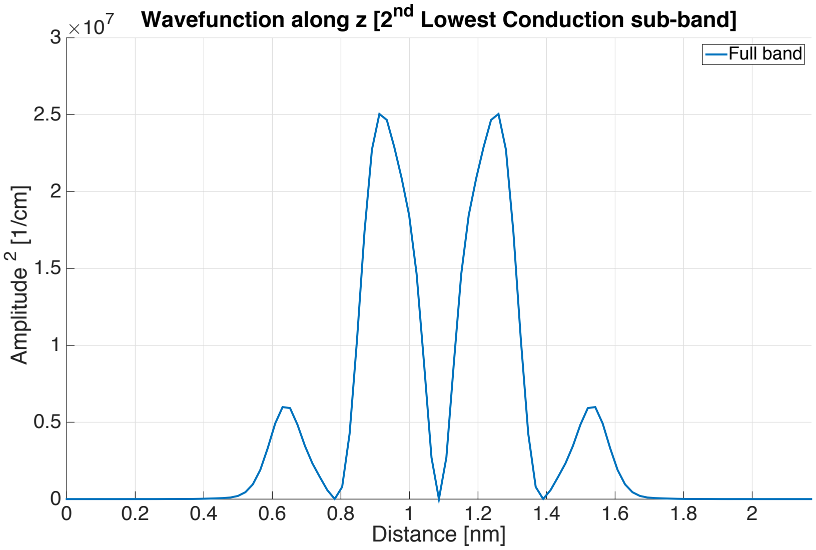

Figure 3.7: 2^{nd} Lowest Conduction Sub-band: 1.08 nm [100] Si Film

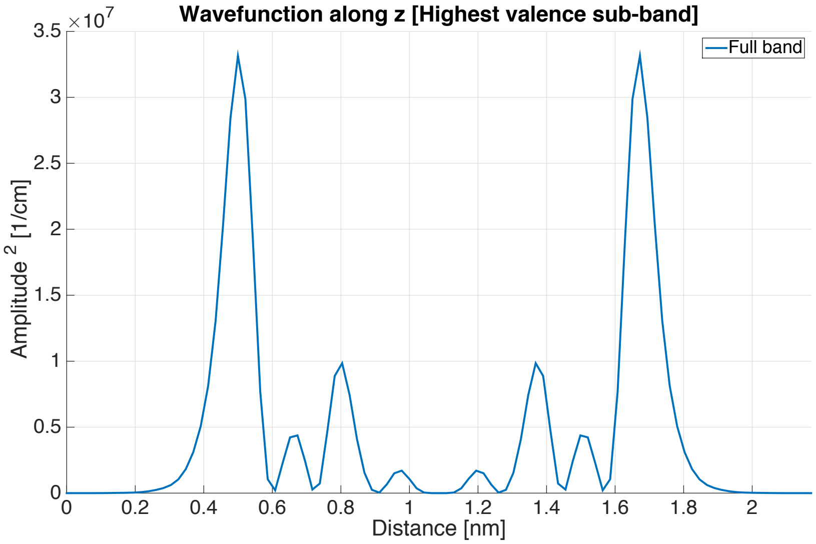

Figure 3.8: Highest Valence band: 1.08 nm [100] Si Film

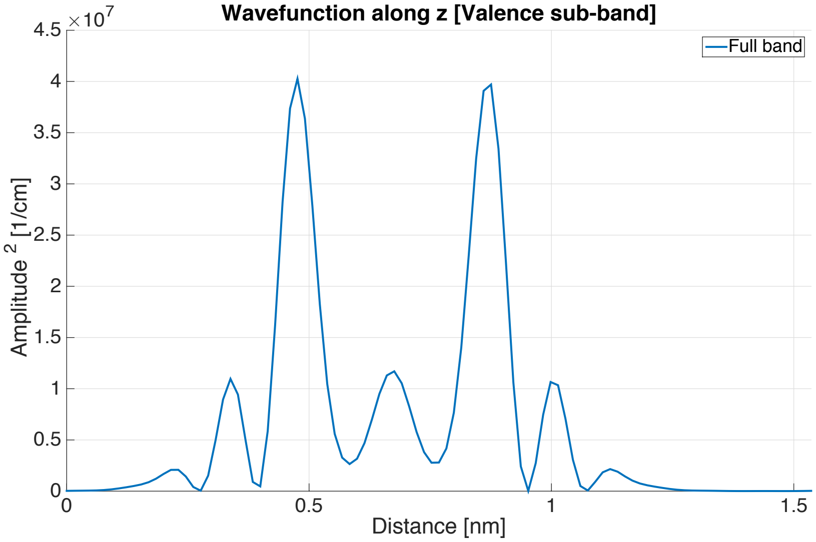

Figure 3.9: Highest Valence band: 0.769 nm [110] Si Film

Chapter 4

SELF CONSISTENT SCHRODINGER POISSON SOLVER

4.1 Poisson Solver

Once the electron and hole carrier concentrations are computed, the next step is to solve the Poisson equation to find the resulting potential in the channel due to charge carriers. Since we have confinement in the z-direction and we are studying the equilibrium characteristics of DG SOI MOS Capacitors, we need to solve the Poisson equation only in the confinement direction, of the form:

$$\begin{aligned} &\frac{\partial}{dz}\left[\boldsymbol{\epsilon_r(z)}\frac{\partial\boldsymbol{\phi(z)}}{dz}\right] = \frac{\boldsymbol{\rho(z)}}{\epsilon_0} \\ &\boldsymbol{\rho}(z) = (p(z) - n(z) + N_d(z) - N_a(z)); \\ &\text{z is the direction of confinement.} \end{aligned} \tag{4.1}$$

The electron and hole concentrations computed in Eq.(3.11) depend implicitly on potential energy $\phi = -eV_{channel}$ along the channel. ϕ affects the bandstructure by shifting the energy levels with respect to unbiased Fermi energy level ($E_{i,n} \rightarrow E_{i,n} - q\phi$) which in turn causes the change in carrier concentrations. For the purpose of our work we approximate ϕ dependance to be exponential [29, 37, 38]. Therefore the carrier concentration expressions can be rewritten as described in Eq.(4.2)

$$\begin{aligned} &p(z) = \sum_{\boldsymbol{i}}\sum_{\boldsymbol{n^{VB}}} D(E_{i,n})(1 - f(E_{i,n}))|\psi(z)|^2 \exp\left(-\frac{\phi(z)}{V_T}\right) \\ &n(z) = \sum_{\boldsymbol{i}}\sum_{\boldsymbol{n^{CB}}} D(E_{i,n})(f(E_{i,n}))|\psi(z)|^2 \exp\left(\frac{\phi(z)}{V_T}\right) \\ &\text{in Eq.(4.2) CB corresponds to conduction band and VB corresponds to valence band.} \end{aligned} \tag{4.2}$$

To solve the Eq.(4.1) numerically, we need to discretize the equation where $\boldsymbol{\phi}(z)$ is the spatially varying potential and $\boldsymbol{\rho}$ is the spatially varying net charge disribution. Discretization of the equation would help to transform the differential equation problem into system of algebraic equations. The following section discusses the discretization of the Poisson equation Eq.(4.1) for spatially varying dielectric constant and non-uniform meshing. These discretization formulae can be easily extended to the case of uniform meshing and dielectric constant. Figure (4.1) represents the device being simulated. The poisson equation is solved for the entire structure including the vacuum layers.

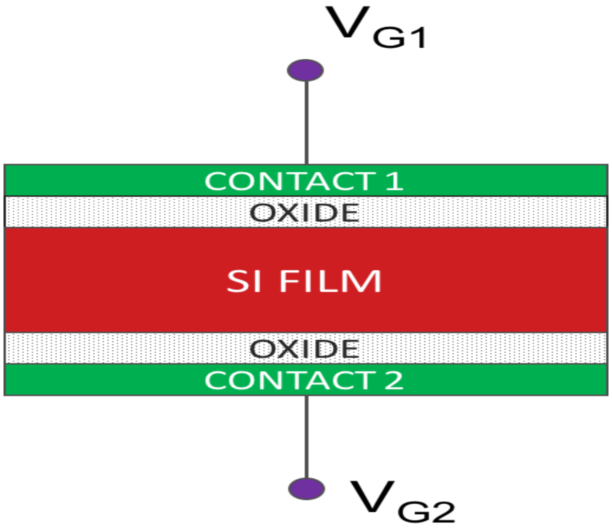

Figure 4.1: Simulated Device Geometry

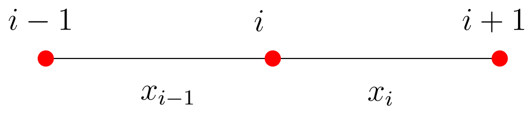

Figure 4.2: 3 Point Stencil for Finite Difference Discretization

Figure Courtesy @ [39]

4.1.1 Discretizing the Poisson's Equation

To discretize the derivative we adopted the central difference scheme. Fig.(4.2) represents the 3 points stencil for the chosen grid and x_i is the grid size at mesh point$[i]$. The device is assumed to span from $i = 1 \cdots N$ node points and boundary conditions are applied at mesh point $i = 0$ and $i = N + 1$. The potential value at the boundary conditions is dependent upon the voltage applied at those points. Then for the device region:

$$\begin{aligned} \frac{\partial}{dz}\left(\boldsymbol{\epsilon^r}(z)\frac{\partial\phi}{dz}\right) &= \frac{\boldsymbol{\epsilon^r_{i+1/2}}\frac{\partial\phi}{dz}|_{i+1/2} - \boldsymbol{\epsilon^r_{i-1/2}}\frac{\partial\phi}{dz}|_{i-1/2}}{0.5(z_i + z_{i-1})} = \frac{\rho}{\epsilon_0} \\ &\because \text{for the work presented in thesis uniform mesh is used} \\ &\therefore z_i = z_{i-1} = \Delta z \end{aligned} \tag{4.3}$$

From Eq. (4.3) for uniform mesh we arrive at

$$\begin{aligned} \frac{\partial}{dz}\left(\boldsymbol{\epsilon^r}(z)\frac{\partial\phi}{dz}\right) &= \frac{\epsilon^r_{i+1/2}\left(\frac{\phi_{i+1}-\phi_i}{\Delta z}\right) - \epsilon^r_{i-1/2}\left(\frac{\phi_i-\phi_{i-1}}{\Delta z}\right)}{\Delta z} \\ &= \frac{\rho_i}{\epsilon_0} \\ &= \frac{\left(\frac{\epsilon_i+\epsilon_{i+1}}{2}\right)\left(\frac{\phi_{i+1}-\phi_i}{\Delta z}\right) - \left(\frac{\epsilon_i+\epsilon_{i-1}}{2}\right)\left(\frac{\phi_i-\phi_{i-1}}{\Delta z}\right)}{\Delta z} \\ &= \frac{\left(\epsilon^r_{i+1}+\epsilon^r_i\right)\phi_{i+1} - \left(\epsilon^r_{i+1}+\epsilon^r_{i-1}+2\epsilon^r_i\right)\phi_i + \left(\epsilon^r_i+\epsilon^r_{i-1}\right)\phi_{i-1}}{2(\Delta z)^2} \\ &= \frac{\rho_i}{\epsilon_0} \end{aligned} \tag{4.4}$$

Eq.(4.4) represents a system of linear equations whose solution yield the potential along the channel. Then

$$\lceil A \rceil \phi = B \tag{4.5}$$

In Eq.(4.5) A is the co-efficient matrix , ϕ is the potential vector and B is the forcing function, of the form:

$$A = \begin{pmatrix} -\beta_{1,1} & \alpha_{1,2} & & 0 \\ \gamma_{2,1} & \ddots & \ddots & \\ & \ddots & \ddots & \alpha_{N-1,N} \\ 0 & & \gamma_{N,N-1} & -\beta_{N,N} \end{pmatrix}.$$

$$B = \begin{pmatrix} \rho_1 \\ \rho_2 \\ \vdots \\ \rho_N \end{pmatrix}.$$

From Eq.(4.4) for the i^{th} node we have

$$\begin{aligned} \beta_{i,i} &= -\Big(\epsilon^r_{i+1} + \epsilon^r_{i-1} + 2\epsilon^r_i\Big) \\ \alpha_{i,i+1} &= \Big(\epsilon^r_{i+1} + \epsilon^r_i\Big) \\ \gamma_{i-1,i} &= \Big(\epsilon^r_i + \epsilon^r_{i-1}\Big) \\ \rho_i &= (p(i) - n(i) + N_d(i) - N_a(i)) \end{aligned} \tag{4.6}$$

This system of algebraic equations is linear and has to be solved self consistently with in Schrodinger solver to find the self consistent potential and charge distribution in the structure of interest.

4.1.2 Linearizing Forcing Function

Under equilibrium conditions the mobile charge concentration is given by Eq.(4.2) If we change $\phi_{new} \Rightarrow \phi_{old} + \delta$ the corresponding change in the concentrations is calculated from :

$$\begin{aligned}
&n(z) = n^{''}(z)\exp\left(-\frac{\phi_{old}+\delta}{V_T}\right);\\
&where\, n^{''} = \sum_{\boldsymbol{i}}\sum_{\boldsymbol{n^{CB}}} D(E_{i,n})(f(E_{i,n}))|\psi(z)|^2\\
&p(z) = p^{''}(z)\exp\left(\frac{\phi_{old}+\delta}{V_T}\right);\\
&where\, p^{''} = \sum_{\boldsymbol{i}}\sum_{\boldsymbol{n^{VB}}} D(E_{i,n})(1-f(E_{i,n}))|\psi(z)|^2
\end{aligned} \tag{4.7}$$

Assuming $\frac{\delta}{V_T} \ll 1$ we can write Eq.(4.7) as

$$\begin{aligned}
&\because \exp(x) \approx 1 + x \text{ when } |x| \ll 1\\
&n(z) = n^{''}(z)\exp\left(-\frac{\phi_{old}}{V_T}\right)(1-\frac{\delta}{V_T})\\
&p(z) = p^{''}(z)\exp\left(\frac{\phi_{old}}{V_T}\right)(1+\frac{\delta}{V_T})\\
\therefore \frac{\rho}{\epsilon_0} &= -n^{''}(z)\exp\left(-\frac{\phi_{old}}{V_T}\right)(1-\frac{\delta}{V_T}) + p^{''}(z)\exp\left(\frac{\phi_{old}}{V_T}\right)(1+\frac{\delta}{V_T}) \qquad (4.8)\\
&- N_a + N_d\\
&= \frac{q}{\epsilon_0}(-n^{''}(z)\exp\left(-\frac{\phi_{old}}{V_T}\right) + p^{''}(z)\exp\left(\frac{\phi_{old}}{V_T}\right)\\
&\frac{\delta}{V_T}(n^{''}(z)\exp\left(-\frac{\phi_{old}}{V_T}\right) + p^{''}(z)\exp\left(\frac{\phi_{old}}{V_T}\right)) + -N_a + N_d
\end{aligned}$$

Using Eq.(4.7), Eq.(4.2), Eq.(4.8) and $\delta = \phi_{new} - \phi_{old}$ we can write the final form of the forcing functions as:

$$\begin{aligned}\frac{\rho}{\epsilon_0} &= \frac{q}{\epsilon_0}(-n''(z)\exp\left(-\frac{\phi_{old}}{V_T}\right) + p''(z)\exp\left(\frac{\phi_{old}}{V_T}\right) \\ &+ \frac{(\phi_{new} - \phi_{old})}{V_T}(n''(z)\exp\left(-\frac{\phi_{old}}{V_T}\right) + p''(z)\exp\left(\frac{\phi_{old}}{V_T}\right) - N_a + N_d) \\ &= \frac{q}{\epsilon_0}(-n(z) + p(z) - N_a + N_d + \frac{(\phi_{new} - \phi_{old})}{V_T}(n(z) + p(z)))\end{aligned} \tag{4.9}$$

Thus the final linearized form of the poisson equation is :

$$\begin{aligned}&\frac{\left(\epsilon^r_{i+1} + \epsilon^r_i\right)\phi^{new}_{i+1} - \left(\epsilon^r_{i+1} + \epsilon^r_{i-1} + 2\epsilon^r_i\right)\phi^{new}_i + \left(\epsilon^r_i + \epsilon^r_{i-1}\right)\phi^{new}_{i-1}}{2(\Delta z)^2} - \frac{q}{\epsilon}\frac{(n^{old}(z) + p^{old}(z))}{V_T}\phi^{new}_i \\ &= \frac{q}{\epsilon_0}(n^{old}(i) - p^{old}(i) - N_a(i) + N_d(i) - \frac{\phi^{old}_i}{V_T}(n^{old}(i) + p^{old}(i)))\end{aligned} \tag{4.10}$$

$n^{old}(z)$ and $p^{old}(z)$ are the electron and hole concentrations computed according to Eq.(4.2) at $\phi = \phi_{old}$.If Eq.(4.10) ϕ^{old} from the previous itertaion provides feedback for the calculation of ϕ^{new}.This feedback helps in the covergence of potential for higher voltages. Hence, co-efficients of the poisson equation for its linearized form are:

$$\begin{aligned}\beta_{i,i} &= -\frac{\left(\epsilon^r_{i+1} + \epsilon^r_{i-1} + 2\epsilon^r_i\right)}{2\Delta z^2} - \frac{q}{\epsilon}\frac{(n^{old}(i) + p^{old}(i))}{V_T} \\ \alpha_{i,i+1} &= \frac{\left(\epsilon^r_{i+1} + \epsilon^r_i\right)}{2\Delta z^2} \\ \gamma_{i-1,i} &= \frac{\left(\epsilon^r_i + \epsilon^r_{i-1}\right)}{2\Delta z^2} \\ \rho_i &= (p^{old}(i) - n^{old}(i) + N_d(i) - N_a(i)) - \frac{\phi^{old}_i}{V_T}(n^{old}(i) + p^{old}(i)))\end{aligned} \tag{4.11}$$

Once the Poisson equation solver is setup, the next step is to self-consistently couple it with the full band schrodinger equation to get potential and charge distributions. The following section describes the flowchart of the afore mentioned self consistent process. At first we need to calibrate the device for zero external voltage and determine the Fermi energy level. This Fermi energy level is assumed to be constant throughtout the device since we are analyzing device under equilibrium conditions. Depending on the external gate voltage the boundary conditions for the device would change. Fermi energy level in the channel stays constant through all the iterations and the bands move relative to the fermi energy depending on the channel potential.

$$\begin{aligned} \phi(0)[eV] &= -V_l \\ \phi(N+1)[eV] &= -V_r \end{aligned} \tag{4.12}$$

In Eq.(4.12) V_l and V_r are gate voltages applied on the left and right contacts respectively This modifies the forcing function as follows:

$$B = \begin{pmatrix} \rho_1 + \dfrac{\epsilon(1)V_l}{2dz^2} \\ \rho_2 \\ \vdots \\ \rho_N + \dfrac{\epsilon(N)V_r}{2dz^2} \end{pmatrix}.$$

4.2 Self Consistent Schrodinger Poisson Solver Flowchart

4.2.1 Device Calibration at $V_l = V_r = 0$

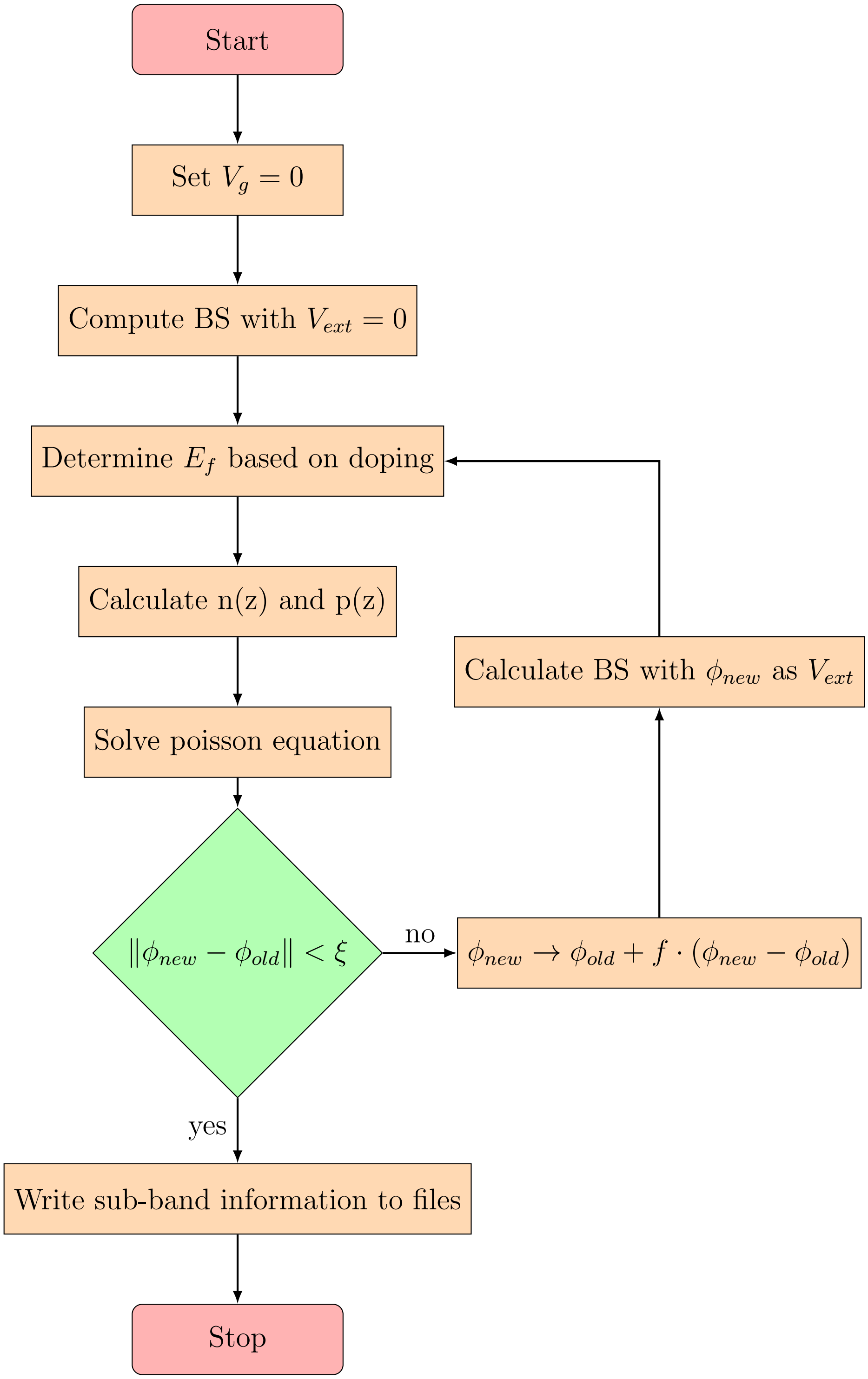

4.2.2 Self Consistent Solution for $V_l = V_r \neq 0$

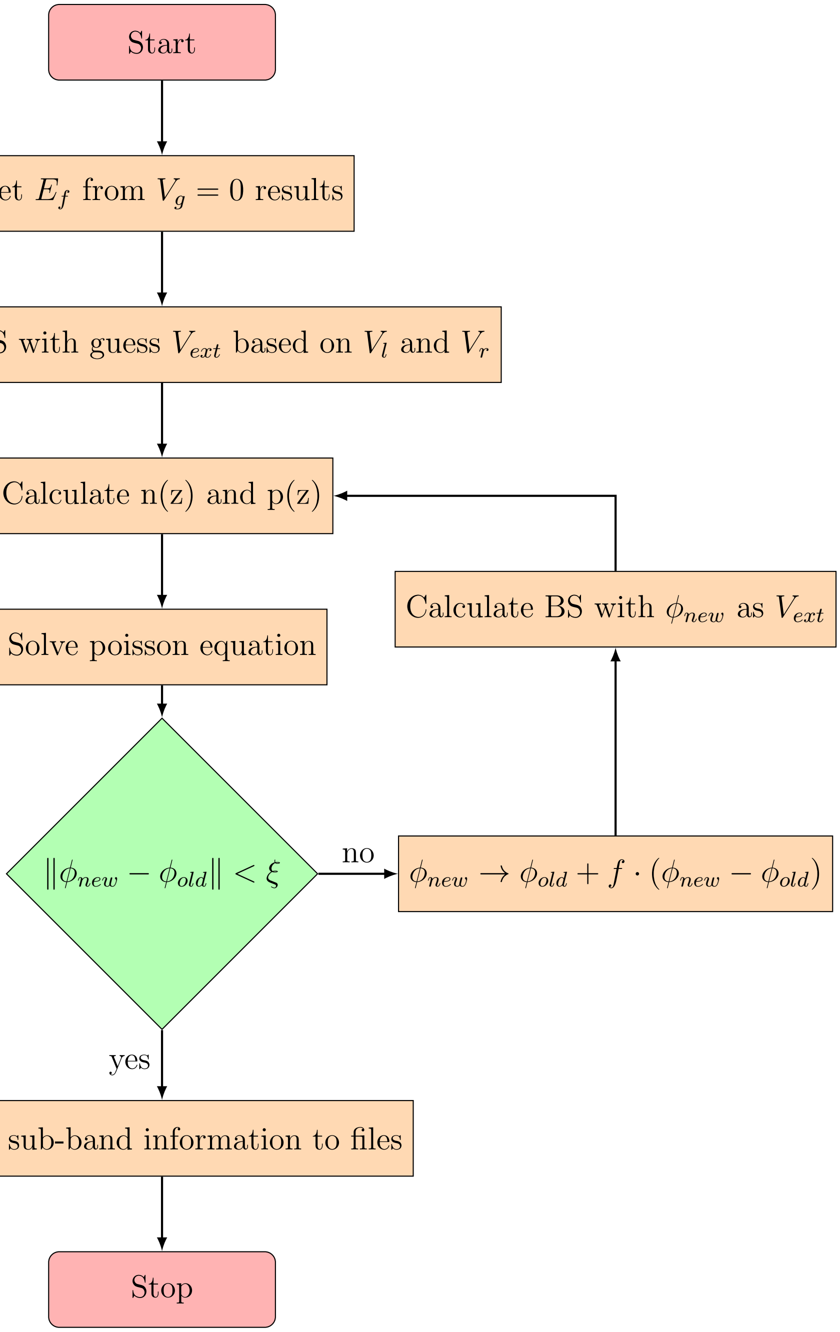

The acronym BS in Fig.(4.2.1) and Fig.(4.2.2) refers to full band structure calculation whereas E_f refers to the Fermi energy. ξ represents the tolerance used for covergence. The weighted average factor f can be fixed or variable and $0 \leq f \leq 1$.

Chapter 5

RESULTS AND CONCLUSION

5.1 DG SOI MOS Capacitor

5.1.1 Variation of Sheet Charge Density With Gate Voltage

Fig.(5.1) shows the variation of sheet charge density with the applied gate voltage for UTB n-MOSFET SOI devices. The Si film for both the wafer orientations was doped p-type with the doping density of 1e19$[cm^{-3}]$. It suggests that the threshold voltage is $\approx$ 1.47V for [100] oriented Si film whereas it is $\approx$ 1.34V for [110] orientation. The difference in threshold voltage can be attributed to difference in the bandgap values for Si films with different wafer orientation, where it is 1.78 eV for 1.08 nm

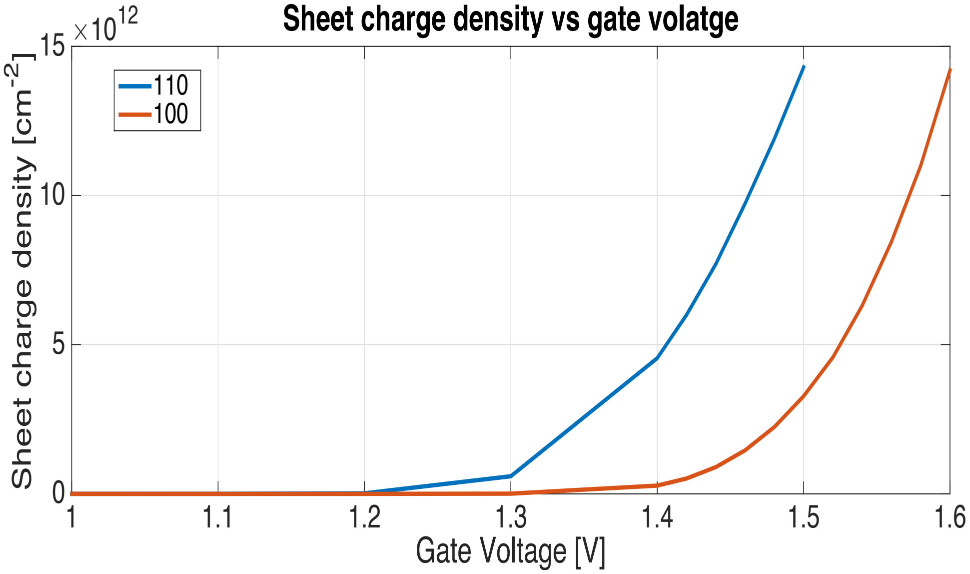

Figure 5.1: Sheet Charge Density vs Gate Voltage: 1.08 nm [100] and 1.15 nm [110] Si Films

[100] Si film and 1.58 eV for 1.15 nm [110] Si film. Hence, as the bandgap for [100] Si film is higher than its [110] counterpart it needs more gate voltage to invert the channel.

5.1.2 Variation of Channel Potential

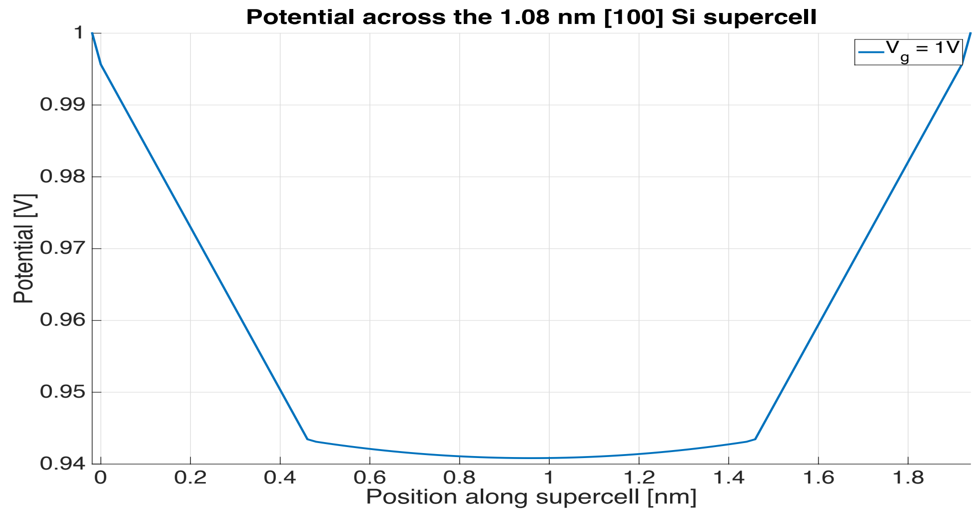

Figure 5.2: Potential Along Confinement: [100] Si Film

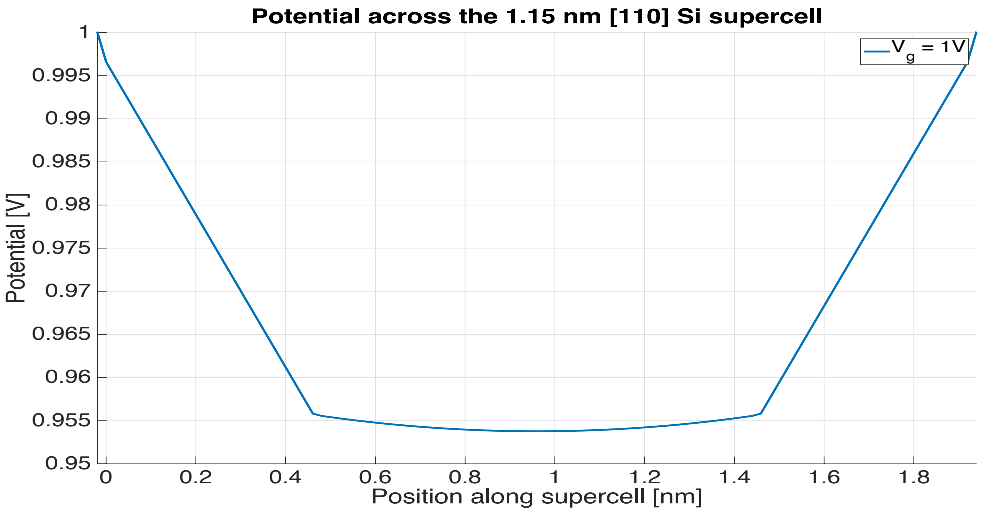

Figure 5.3: Potential Along Confinement: [110] Si Film

The potentialvariation along the channel is nearly parabolic and negligible(due to small thickness) as seen in Fig.(5.3). Fig.(5.2), Fig.(5.3) and Fig.(5.4)represent the self consistent results for gate voltage $V_l = V_r = 1V$. As can seen in Fig.(5.4) and Fig.(5.5) the Si channel is volume inverted. Also the charge is more confined for [100] orientation as compared to its [110] counterpart. Volume inversion leads to mobility improvement for carriers in DG SOI channel as compared to SG SOI; (they suffer less surface scattering due to charge being peaked in the centre of channel [40]). Among the wafer orientations we find that added confinement for [100] Si film might lead to decrease in scattering based mobility reduction.

5.1.3 Charge Distribution Profile

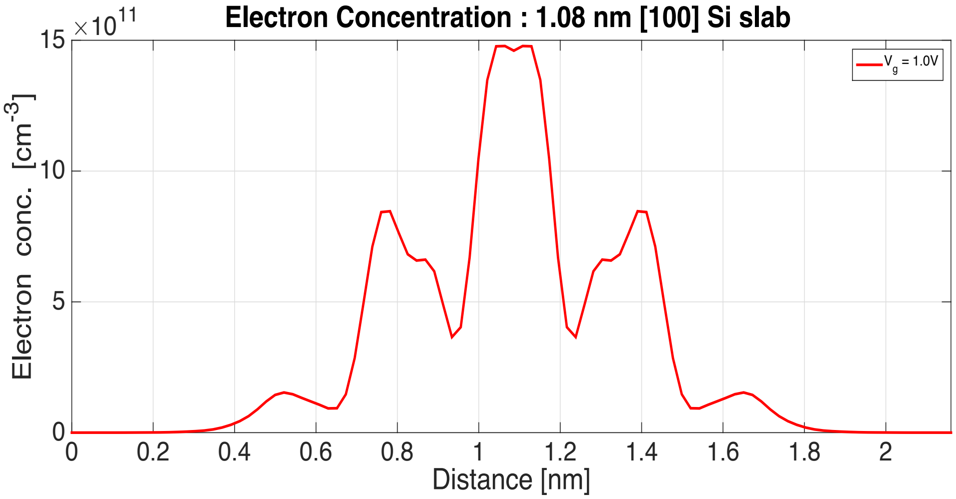

Figure 5.4: Charge Distribution Across the Si Film: [100] Orientation

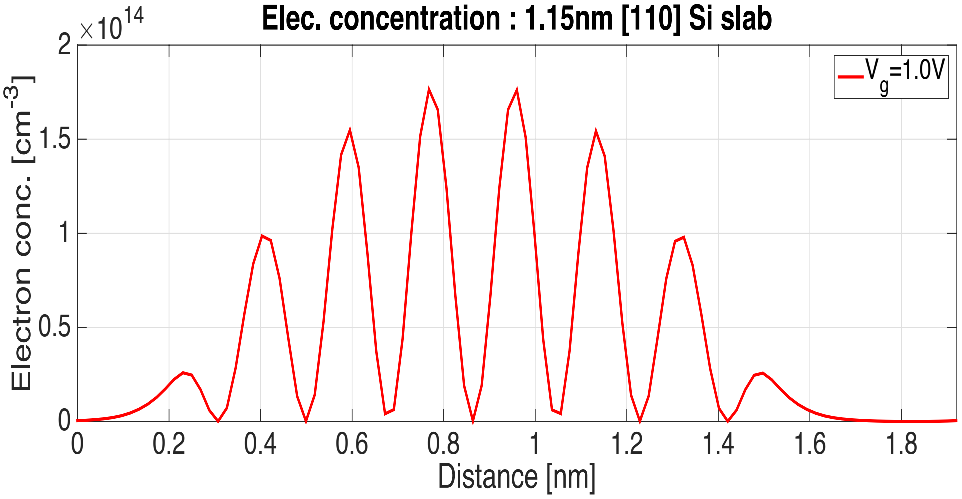

Figure 5.5: Charge Distribution Across the Si Film: [110] Orientation

5.2 Conclusion and Future Works

This thesis has successfully coupled the empirical pseudopotential based full band approach with the poisson solver. The simulator is capable of simulating UTB SOI devices for two important crystallographic orientation of silicon namely [100] and [110]. The bandstructure analysis of [100] and [110] oriented Si thin films revealed interesting thickness dependent behaviour.

Confined si slabs were found to behave as direct bandgap material for [100] crystallographic orientation. This behaviour is observed for lower thickness range mainly sub 10nm. This is direct consequence of confinement due to ultra thin silicon channel. [110] Si slabs behave as direct bandgap for thicknesses $<$ 1.15nm and for higher thickness range it transitions into an indirect bandgap material. [110] Si films have lower bandgap than [100] Si films for similar value of slab thickness. Thus we could establish that confinement effects are more pronounced in [100] crystallographic direction as compared to [110]. It is because of the non-alignment of axes of constant energy surfaces with the device axes for [110] orientation.

Threshold voltage for UTB SOI at a given value of doping is predicted to increase with decrease in the thickness. This is due to band gap widening effect caused by quantum confinement. Since thickness of Si slabs is very small it leads to volume inverted channels. Both [100] and [110] are capable of achieving higher electron concentrations before entering the degenerate statistical regime. Hence, [100] and [110] UTB SOI MOSFET are very important from the technological point of view as they are suitable to continue the Moore's law scaling.

In the present work wavefunctions obtained from EPM are approxiated to be independent of in-plane wavevector K. This approximation can be relaxed to develop more accurate full band schrodinger poisson solver. Accuracy of the solver can be enhanced by incorporating the effects of oxide thickness on the device behaviour by considering oxygen pseudopotentials. Thus new supercell has to be determined by the placement of oxygen atoms in the supercell. Nonetheless it would lead to increase in the scale of the EPM problem. Since full band calculations accuarately describe the density of states they can more accurately calculate the scattering rates. Thus full band EPM technique can be coupled with Monte Carlo method to accurately describe the mobility of carriers in channel.

Simulator developed as a part of thesis work can also help in analyzing equilibrium properties of heterostructures like superlattices. We aim to deploy the simulation tool as FUUL-BAND SCHRED 2.1 on `www.nanohub.org` which will be capable of doing self consistent full band calculations mainly for heterostructures and UTB SOI geometries. Eventually I will provide some useful insights into [100] and [110] DG UTB SOI architectures.

REFERENCES

[1] Wang, L. W. and A. Zunger, "Electronic structure pseudopotential calculations of large (. apprx. 1000 atoms) si quantum dots", The Journal of Physical Chemistry **98**, 8, 2158–2165 (1994).

[2] Brock, D. C. and G. E. Moore, *Understanding Moore's law: four decades of innovation* (Chemical Heritage Foundation, 2006).

[3] "After moore's law", Technology quarterly, The Economist, `http://www.economist.com/technology-quarterly/2016-03-12/after-moores-law` (2016).

[4] "Itrs report", Tech. rep., SEMATECH, `https://www.dropbox.com/sh/0ce36nq4118wiag/AACZ1MVxbt8GBSPlla7-FoMda?dl=0&preview=1_ExecSum2003.pdf` (2003).

[5] Courtland, R., "Transistors could stop shrinking in 2021", Tech. rep., IEEE, `http://spectrum.ieee.org/semiconductors/devices/transistors-could-stop-shrinking-in-2021` (2016).

[6] Shahidi, G. G., "Soi technology for the ghz era", in "VLSI Technology, Systems, and Applications, 2001. Proceedings of Technical Papers. 2001 International Symposium on", pp. 11–14 (IEEE, 2001).

[7] Mazure, C., G. Celler, C. Maleville and I. Cayrefourcq, "Advanced soi substrate manufacturing", in "Integrated Circuit Design and Technology, 2004. ICICDT'04. International Conference on", pp. 105–111 (IEEE, 2004).

[8] Shepard, K. L. and D.-J. Kim, "Body-voltage estimation in digital pd-soi circuits and its application to static timing analysis", IEEE Transactions on Computer-Aided Design of Integrated Circuits and Systems **20**, 7, 888–901 (2001).

[9] Vasileska, D., "Theory and silvaco modeling of soi devices", (2014).

[10] Dr.Fikru.Adamu-Lema, "Scaling of silicon on insulator", `http://userweb.eng.gla.ac.uk/fikru.adamu-lema/Chapter_06.pdf` (2005).

[11] K. M., J. S. L. B. R. S. R. F., G. Grula and P. Skerry, IEDM Tech. Dig. pp. 583–586 (1997).

[12] Chang, L., Y.-k. Choi, D. Ha, P. Ranade, S. Xiong, J. Bokor, C. Hu and T.-J. King, "Extremely scaled silicon nano-cmos devices", Proceedings of the IEEE **91**, 11, 1860–1873 (2003).

[13] Tsutsui, G., M. Saitoh and T. Hiramoto, "Experimental study on superior mobility in [110]-oriented utb soi pmosfets", IEEE electron device letters **26**, 11, 836–838 (2005).

[14] Tsutsui, G. and T. Hiramoto, "Mobility and threshold-voltage comparison between [110]-and (100)-oriented ultrathin-body silicon mosfets", IEEE Transactions on Electron Devices **53**, 10, 2582–2588 (2006).

[15] Lucci, L., P. Palestri, D. Esseni, L. Bergagnini and L. Selmi, "Multisubband monte carlo study of transport, quantization, and electron-gas degeneration in ultrathin soi n-mosfets", IEEE Transactions on Electron Devices **54**, 5, 1156–1164 (2007).

[16] Ren, Z., R. Venugopal, S. Goasguen, S. Datta and M. S. Lundstrom, "nanomos 2.5: A two-dimensional simulator for quantum transport in double-gate mosfets", IEEE Transactions on Electron Devices **50**, 9, 1914–1925 (2003).

[17] Lundstrom, M. and J. Guo, "Nanoscale transistors: device physics, modeling and simulation", (2006).

[18] Zhang, S. B., C.-Y. Yeh and A. Zunger, "Electronic structure of semiconductor quantum films", Phys. Rev. B **48**, 11204–11219, URL `http://link.aps.org/doi/10.1103/PhysRevB.48.11204` (1993).

[19] Klimeck, G. and M. Luiser, "Scattering in si-nanowires?where does it matter?", in "2010 Silicon Nanoelectronics Workshop", pp. 1–2 (IEEE, 2010).

[20] Perdew, J. P. and A. Zunger, "Self-interaction correction to density-functional approximations for many-electron systems", Phys. Rev. B **23**, 5048–5079, URL `http://link.aps.org/doi/10.1103/PhysRevB.23.5048` (1981).

[21] Slater, J. C., "A generalized self-consistent field method", Phys. Rev. **91**, 528–530, URL `http://link.aps.org/doi/10.1103/PhysRev.91.528` (1953).

[22] Pauli, W., "Exclusion principle, lorentz group and reflexion of space-time and charge", Niels Bohr and the development of physics **1**, 30 (1955).

[23] Guzzo, M., M. Gatti and L. Reining, *Exchange and correlation effects in the electronic properties of transition metal oxides: the example of NiO*, Master's thesis, Università degli studi di Milano-Bicocca (2008).

[24] H.Bethe, "Quantenmechanik der ein- und zwei-elektronenprobleme", **24/2** (1933).

[25] Herring, C., "A new method for calculating wave functions in crystals", Phys. Rev. **57**, 1169–1177, URL `http://link.aps.org/doi/10.1103/PhysRev.57.1169` (1940).

[26] Fll, P. D. H., "Semiconductors i", `http://www.tf.uni-kiel.de/matwis/amat/semi_en/index.html` (1999).

[27] Quester, W., `https://commons.wikimedia.org/wiki/File:Sketch_Pseudopotentials.png` (2006).

[28] Gamiz, F. and M. Fischetti, “Monte carlo simulation of double-gate silicon-on-insulator inversion layers: the role of volume inversion”, Journal of Applied Physics **89**, 10, 5478–5487 (2001).

[29] Majumdar, K. and N. Bhat, “Bandstructure effects in ultra-thin-body dgfet: A fullband analysis”, arXiv preprint arXiv:1003.5298 (2010).

[30] Guan, X. and Z. Yu, “Fast algorithm for bandstructure calculation in silicon nanowires using supercell approach”, International Journal of Computational Science and Engineering **2**, 3-4, 129–133 (2006).

[31] Ungersbck, S.-E., *Advanced Modeling of Strained CMOS Technology*, Ph.D. thesis, Technischen Universitt Wien (1977).

[32] Fischetti, M. and W. Vandenberghe, *Advanced Physics of Electron Transport in Semiconductors and Nanostructures*, Graduate Texts in Physics (Springer International Publishing, 2016), URL `https://books.google.com/books?id=gu80DAAAQBAJ`.

[33] Wayner, D. D. and R. A. Wolkow, “Organic modification of hydrogen terminated silicon surfaces 1”, Journal of the Chemical Society, Perkin Transactions 2 , 1, 23–34 (2002).

[34] Lu, Z. and D. Grozea, “Crystalline si/sio2 quantum wells”, Applied physics letters **80**, 2, 255–257 (2002).

[35] Haug, A., *Theoretical solid state physics* (Pergamon Press, New York, N.Y., 1972).

[36] Gilat, G. and L. Raubenheimer, “Accurate numerical method for calculating frequency-distribution functions in solids”, Physical Review **144**, 2, 390 (1966).

[37] Taur, Y., “An analytical solution to a double-gate mosfet with undoped body”, IEEE Electron Device Letters **21**, 5, 245–247 (2000).

[38] Trellakis, A., A. Galick, A. Pacelli and U. Ravaioli, “Iteration scheme for the solution of the two-dimensional schrödinger-poisson equations in quantum structures”, Journal of Applied Physics **81**, 12, 7880–7884 (1997).

[39] Thulasingam, G. K. J., *SCHRED 2nd Generation ? Tool to Model MOS Capacitors*, Master’s thesis, Arizona State University (2010).

[40] Sverdlov, V., E. Ungersboeck, H. Kosina and S. Selberherr, “Volume inversion mobility in soi mosfets for different thin body orientations”, Solid-State Electronics **51**, 2, 299–305 (2007).

[41] Vasileska, D. and S. M. Goodnick, “Computational electronics”, Synthesis Lectures on Computational Electromagnetics **1**, 1, 1–216 (2005).

APPENDIX A

CALCULATION OF DENSITY OF STATES USING GILAT RAUBENHEIEMR ALGORITHM

As discussed in chapter 3 to compute density of states numerically Gilat Raubenheimer algorithm is employed. Restating Eq.(3.6) the denisty of states (DOS) can be written as:

$$\begin{aligned} g(E) =& \frac{\int_{E=constant} dl}{2\pi^2 \cdot |\nabla_k E|} \\ &= \frac{\sum_{\boldsymbol{j,n}} L(j,n)}{|\nabla_k E|} \\ &\text{L(j,n) is the length of the equienergy contour corresponding to energy E [32]} \\ &\text{intersecting the k-space grid point } k_j \text{ having eigen energy } E_{j,n}; \\ &\text{n is band index} \end{aligned} \tag{A.1}$$

This section discusses the calculation of $L(j,n)$ corresponding to energy E. It is assumed that the intersection of equienergy lines with k-space grid is linear. This assumption can be justified for very small grid spacing.

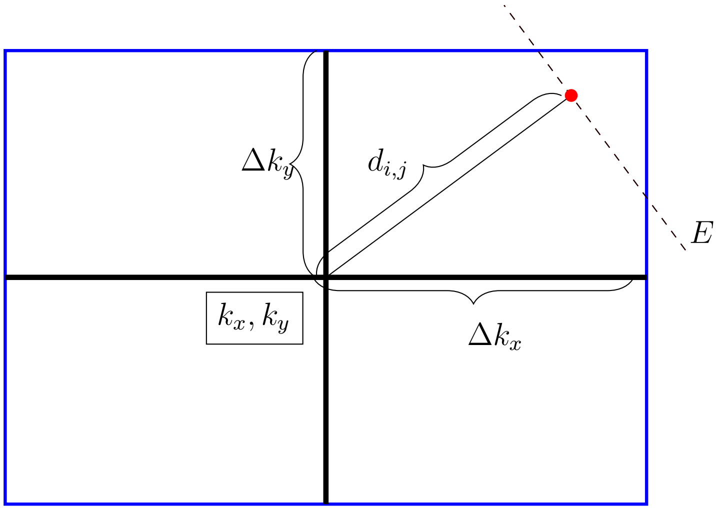

Figure A.1: Rectangular K- Space Grid

In Fig.(A.1) $d_{i,j}$ represents the distance in k-space of the equienergy line corresponding to E from the center of grid cell denoted by k_x, k_y and eigen energy $E_{i,j}$. i, j represent the k-value and the band index respectively. According to Gilat Raubenheimer algorithm[36] the density of states corresponding to energy E contributed by the grid point k_x, k_y in 2D k-space is proportional to the length of the equienergy surface lying in the grid space centered around k_x, k_y.

Firstly the energy span of particular grid point is determined. In other words the range of energy values which would non-zero intersecting length with the grid cell are identified. To do so we need to compute the maximum value of $d_{i,j}$ corresponding to $L_{i,j} = 0$. Assuming the iso energy surface corresponding to E and $E_{i,j}$ are parallel then the gradient at k_x, k_y is also perpendicular to energy surface of E in the grid cell.

$$d_{i,j} = |\nabla_k E|(E - E_{i,j}) \tag{A.2}$$

In Fig.(A.3) $d_{i,j}^{max}$ is corresponds to the energy span of cell. Using basic geometry:

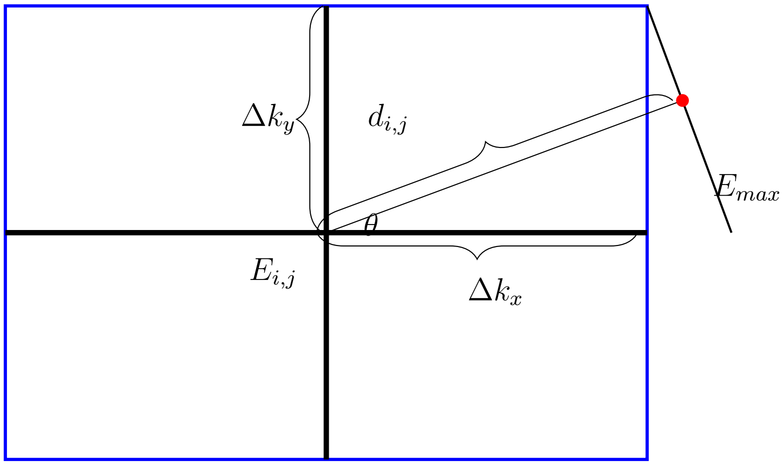

Figure A.2: Energy Span of Grid Cell

$$\begin{aligned}
&\text{Let}\tan(\theta) = |\nabla_k E| \\
&d_{i,j}^{max} = \frac{\Delta K_y}{2}\sin(\theta) + \frac{\Delta K_x}{2}\cos(\theta) \\
&\text{Thus each cell spans in energy range:} \\
&E_{i,j} - d_{i,j}^{max}|\nabla_k E| \leq E \leq E_{i,j} + d_{i,j}^{max}|\nabla_k E|
\end{aligned} \tag{A.3}$$

Having determined the energy span of grid cell we need to identify the grid cells which contrinute to the density of states for particular energy E. Then we calculate $L_{i,j}$ for the chosen grid cells.

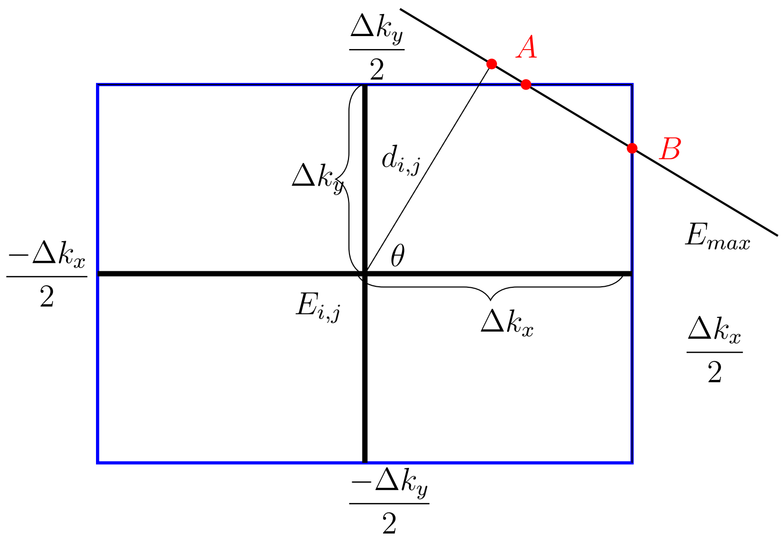

Figure A.3: Density of State Calculation

Since AB is perpendicular to line segment with length $d_{i,j}$ the equation of line is given by:

$$y = -\frac{x}{\tan(\theta)} + \frac{d}{\sin(\theta)} \tag{A.4}$$

The sides of the rectangle grid cell defined in Fig.(A.3) are:

- $x = \pm\frac{\Delta k_x}{2}$
- $y = \pm\frac{\Delta k_y}{2}$

Thus the possible values A and B can take depending on the value of θ are :

- $A = d_{i,j}\cos(\theta) \mp \frac{\Delta k_y \tan(\theta)}{2}, \pm\frac{\Delta k_y}{2}$
- $B = \pm\frac{\Delta k_x}{2}, \frac{d_{i,j}}{\sin(\theta)} \mp \frac{\Delta k_x}{2\tan(\theta)}$

The next step is to identify the co-ordinatess which lie on the grid cell centered around k_x and k_y. Once these are identified then $L_{i,j}$ = Length of segment AB. Next the gradient calulation is done using Eq.(3.9). This method allows the exact calculation of the gradient and thus makes the density of states calculation reliable even for choice of larger grid size. As is depicted in Fig.(A.4) we find that making the k-space grid coarser by factor of 2 does not appreciably affect the DOS calculation thereby reducing the computation time.

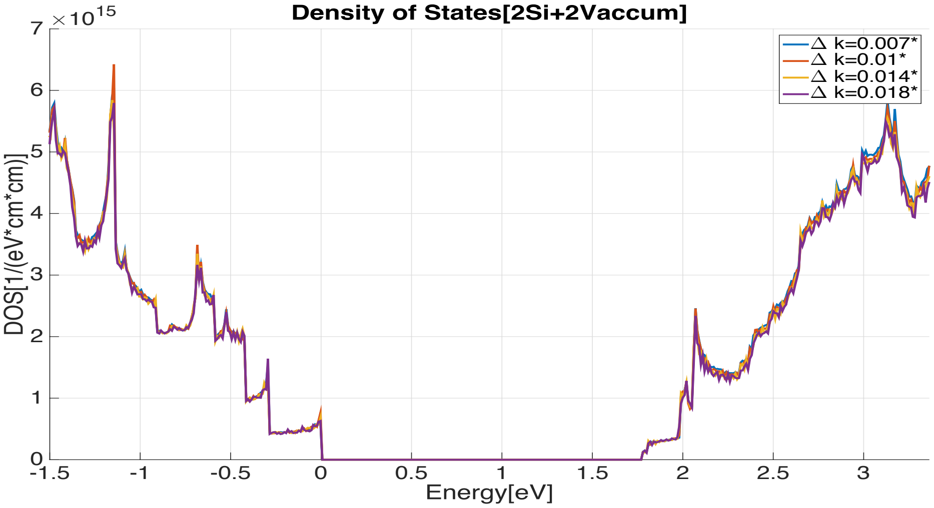

Figure A.4: DOS for Different Grid Sizes

APPENDIX B

VARIABLE POTENTIAL UPDATE PARAMETER

At every iteration of coupled full band schrodinger poisson equation the potential is updated as:

$$\begin{aligned}&\phi_{new} = \phi_{old} + f \cdot (\phi_{new} - \phi_{old}) \\ &\text{where } 0 \leq f \leq 1\end{aligned} \tag{B.1}$$

To improve the rate of convergence we need to consider weighted average of the potential values from two most recent iterations to obtain the best next possible guess for potential [41]. The weighted average factor f can be fixed or relaxed. The adaptive successive over relaxation scheme employed in this work [**?**] is described next:

$$\begin{aligned}&\Delta_i^{max} = max(|\phi_i - \phi_{i-1}|) \\ &f_i = \frac{1}{1 - r_i} \\ &where\, r_i = \frac{\Delta_{i-1}^{max}}{\Delta_{i-2}^{max}} \\ &and\, i\, is\, iteration\, number\end{aligned} \tag{B.2}$$

If $f > 1$ then it is manually set to $f = \frac{1}{\sqrt{2}}$. For smaller thickness of si slabs and double gate architecture the convergence is faster. The Fig.(A.1) shows the convergence of the schrodinger poisson solver for symmetric DG SOI capacitor with $V_g = 0$

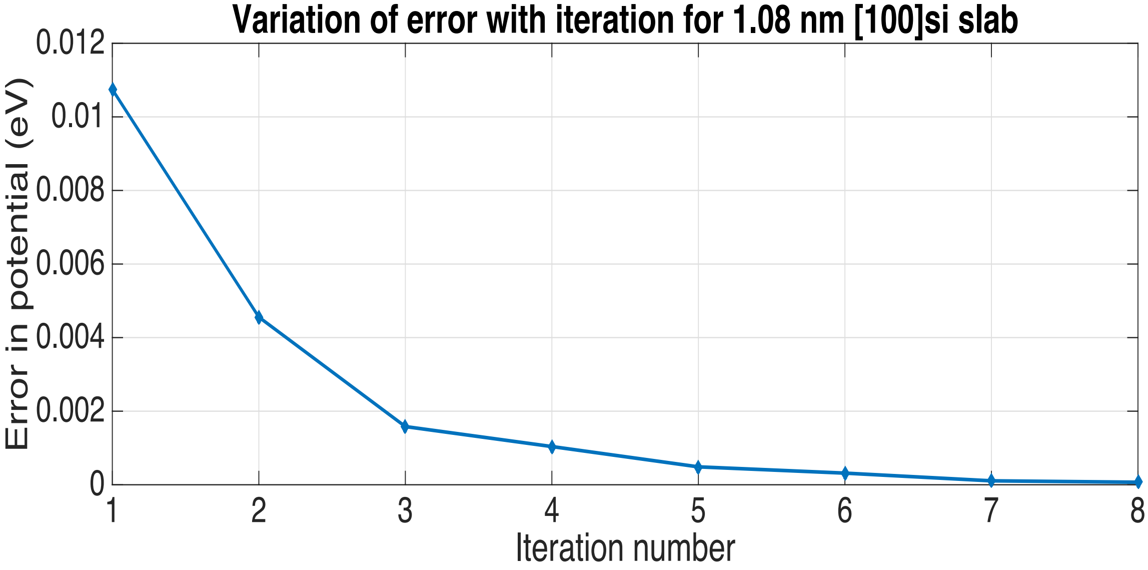

Figure B.1: Potential Error Variation with Iteration